Sedimentology and Geochemistry of a human-induced tufa deposit: implications for palaeoclimatic research

A. Rodríguez-Berriguete[1, 2], A.M. Alonso-Zarza[1, 2], R. Martín-García[1,2] M.C. Cabrera[3],

[1] Dpto. Petrología y Geoquímica, Facultad de Ciencias Geológicas. Universidad Complutense de Madrid. José Antonio Nováis 22, 28040 Madrid, Spain. arberriguete@ucm.es alonsoza@ucm.es;

[2] Instituto de Geociencias (CSIC, UCM), Facultad de Ciencias Geológicas. José Antonio Nováis 12, 28040 Madrid, Spain. alonsoza@ucm.es; arberriguete@ucm.es

[3] Dpto. Física GEOVOL, Campus de Tafira, Universidad de Las Palmas de Gran Canaria, 35017 Las Palmas de Gran Canaria. mcarmen.cabrera@ulpgc.es

ABSTRACT

Geochemical variations across laminated tufas and travertines may reflect the growth style of the carbonate build-up and not just climate-related changes.

This work presents the study of a carbonate deposit, formed on a ravine wall in Gran Canaria Island (Spain), from a broken pipe system used for irrigation of banana plantations. The deposit is a few tens of metres long and has a stepped morphology formed by successive cascade-barriers and pools. Main facies are framestones of coated stems, laminated bindstones, phytoclastic wackestones, and silty mudstones, all of them displaying micritic or coarse crystalline textures.

Lamination from a framestone with coarse crystalline texture was studied from a petrological-sedimentological and geochemical perspective, and water palaeotemperatures were calculated. Lamination displaying five orders of magnitude, from daily to annual or higher, was controlled by the discontinuous supply of water. Lamination consists of crystalline laminae-discontinuity couplets at all observed scales. Estimated mean precipitation rates are 0.7 mm/year, but discontinuity of sedimentation at all lamination orders may have involved greater precipitation rates.

Whereas elemental geochemistry suggests variable conditions but not far from chemical equilibrium, stable isotopes suggest that calcite precipitated under disequilibrium conditions.

However, the small dimensions of the deposit and the relatively high flow velocities allowed lack of $\delta^{13}C$ and $\delta^{18}O$ isotope fractionation in CO_2-HCO_3^- nor in HCO_3^--calcite, leading to independent temperature calculations, both with mean values of 25 °C. Isotopic trends found throughout lamination cannot be explained by strong changes in water temperature nor in $\delta^{13}C_{DIC}$ or $\delta^{18}O_w$. The correction made to eliminate these isotopic trends yielded narrower temperature ranges.

This paper discusses the accuracy of temperature estimations despite of the difficulties coming from disequilibrium and how isotopic trends through time could be explained by the growth of the deposit and not by climate-related changes.

INTRODUCTION

Carbonate spring deposits, including tufa and travertines are terrestrial carbonates whose relatively rapid sedimentation and lithification rate favours the construction of positive reliefs during sedimentation (Pentecost, 2005; Capezzuoli et al., 2014). This rapid growth is the result of the interaction between biotic and abiotic processes (Chafetz and Guidry, 1999; Jones and Peng, 2014). Such interaction between biotic and abiotic processes is focussed on the relation between inorganic $CaCO_3$ precipitation rate and microbial growth rate, the latter being the ability of microbes to grow and/or to move towards a better position as calcite precipitation proceeds (Barton, 2005; Okumura et al., 2011, 2013a).

Tufa and travertine have been studied with the aim to obtain paleoclimate information (Kano et al., 2003; Liu et al., 2006, 2010; Kele et al., 2011; Ibarra et al., 2015). Water palaeotemperature calculations using $\delta^{18}O$ have been improved due to increased information about the disequilibrium conditions commonly occurring in this kind of settings (Kele et al., 2011). In addition, the method of clumped isotope thermometry holds the promise of avoiding some of the difficulties normally encountered in the use of traditional isotope fractionation equations (Eiler, 2011; Kele et al., 2015).

However, complications can arise from the consideration of the various processes causing isotope fractionation which can occur during development of the deposit. Such processes are: speciation of DIC (dissolve inorganic carbon) related to pH and temperature, $CaCO_3$ precipitation rate; and isotope re-equilibration between DIC and water; but also isotope rebalancing between water and air, among many others (Chafetz & Lawrence, 1994; Andrews

et al., 1997; Pentecost, 2005). They also may vary in magnitude or importance through time, related to (seasonal, decadal, etc.) changes in the system such as decreased or increased water flow. This may result in the misinterpretation of the paleoenvironmental signals obtained from these carbonates.

In consequence, the most complete system dynamics information possible should be attained before making inferences from stable isotope data, through sedimentological and petrological analyses, combined with geochemical data.

Laminated sediments and rocks are one of the main targets in sedimentary geology, especially in those works with paleoclimate goals (Kano et al., 2003; Hori et al., 2009; Kawai et al., 2009; Liu et al., 2006, 2010; Okumura et al., 2011, 2012, 2013a, b). However, much more should be learnt about the formation of these laminations in travertine and tufa depositing systems, before such data can be used in palaeoclimate research.

In this paper we present the study of a tufa deposit formed due to human activity in a volcanic setting from groundwater irrigation of banana plantations. Petrological and geochemical features of a laminated sample were studied in detail. The relation between the data obtained and climate is discussed herein. Our results shed some light on limitations and possibilities of the use of tufas and travertines as palaeoclimate archives.

GEOLOGICAL AND HYDROGEOLOGICAL SETTING

Gran Canaria Island, in the central part of Canary Islands (Fig. 1), has a nearly circular shape of about 45 km in diameter and a maximum altitude of 1,949 m in its centre. A dense radial network of deep ravines (known in the local toponomy as *barrancos*) dissecting the island form a rugged topography. The island has a humid northern part due to the influence of the wet trade winds intersected.

Island construction is related to a hot spot located in the African plate, started 14.5 Ma ago (Miocene) with eruption of basaltic to phonolitic materials, continued until the Holocene interspersed with several inactive volcanic periods. Concerning hydrogeology, the island core, of a low permeability, is covered and surrounded by younger, more permeable, heterogeneous volcanic rocks and sediments. Groundwater flows from the recharge areas in the highest and medium high areas towards the coast. Under natural conditions, discharge occurs either to the

sea or into the *barrancos* where the piezometric level intersects the surface (Custodio, 1985; Custodio and Cabrera, 2013). Groundwater, the island's most important natural water resource, has been intensively exploited by means of deep, large diameter shaft wells and water galleries, from the 1920s, continuously drawing down the water level, and almost completely drying up the natural springs (Custodio and Cabrera, 2013). Transportation of water from the producing wells or water galleries (normally located in high lands) to agricultural areas in the coastal plains has led to the existence of a broad network of canals and pipes (Santamarta Cerezal, 2013).

Groundwaters of the northern part of Gran Canaria generally have temperatures of 20 to 25 °C, but some may be higher than 30 °C (SPA-15, 1975; Gasparini et al., 1990). Groundwater quality is highly variable, from low mineral content in the high areas to brackish in the dry parts, being controlled by climate and soil (Custodio and Cabrera, 2008).

Chloride content varies from less than 30 mg/L in the recharge areas, to up to even more 2000 mg/L in the coastal areas. Bicarbonate content increases as the groundwater flows towards the coast. Ca^{2+}, Mg^{2+}, and Na^{+} are the most abundant cations, together with Si^{4+} and, in lower amounts, Mn^{2+} and Fe^{2+} (SPA-15, 1975; Gonfinatini et al., 1976; Gasparini et al., 1990). Sodium is often the dominant cation under natural conditions, but sulphate and nitrate excesses attributed to anthropic contamination, can be also found in the coastal areas (Custodio and Cabrera, 2008).

CO_2-rich groundwaters appear in small areas close to the coast (SPA-15, 1975; Rodríguez-Berriguete, 2017). Their CO_2 contents are commonly higher than 75 mg/l, even exceeding contents of 600 mg/l (SPA-15, 1975; Gasparini et al., 1990).

Groundwaters of the northern part of Gran Canaria commonly have $\delta^{18}O$ values ranging from -3.0 to -4.5 ‰ VSMOW, although slightly higher and lower values than those of that range have been reported (Gonfiantini et al., 1976; Custodio et al., 1987; Gasparini et al., 1990). Dissolved inorganic carbon (DIC) from groundwaters of Gran Canaria display $\delta^{13}C$ values commonly ranging from -2 to -8 ‰ VPDB, although values lower than -10 ‰ have also been reported (Albert et al., 1986; Custodio et al., 1987; Gasparini et al., 1990).

Natural carbonate spring deposits (e.g. Azuaje, Berrazales and Temisas) occurred mostly (but not exclusively) in the northern half of the island. Their formation seems to involve endogenous CO_2 (Rodríguez-Berriguete et al., 2012; Camuera et al., 2014; Estrella de Pinho et al., 2015), regardless of the tufa or travertine facies that may or may not be associated. In

consequence, these deposits are classified as thermogene carbonates because of their positive $\delta^{13}C$ values, according to Pentecost (2005). The three above-mentioned carbonate build-ups are recent but from naturally fed spring deposits, whereas El Calabozo system studied in this paper was fed by an irrigation system pipe. The Calabozo carbonate deposit, on the western slope of the Calabozo ravine (NW Gran Canaria Island), overlays a Miocene phonolitic substrate (Fig. 1C).

METHODS

Thirty five carbonate samples were taken from the more representative facies. Conventional optical petrography studies were performed on 20 thin sections partially stained with red Alizarin Red S. The more fragile samples were submerged in an epoxy resin. An Olympus BX51 optical microscope with an Olympus U-TVO.5XC-3 camera incorporated was used for the study. The mineralogical characterization of sixteen powdered samples from selected facies were analysed, using Phillips PW-1710 X-ray diffraction (XRD) system operating at 40 kV and 30 mA, employing monochromated CuKα radiation.

SEM observations were carried out on 6 gold-coated samples using three microscopes: 1) JEOL JSM-6400 of the ICTS-CNME Luis Brú of Complutense University of Madrid (Spain) working at 20kV, 2) JEOL JSM-820 of the CAI of geological techniques of Complutense University of Madrid (Spain) working at 20 kV and 3) FEI QUANTA 200 apparatus of the MNCN (CSIC) Laboratories working at 30 kV.

Samples for stable isotope analyses were obtained: a) by drilling selected areas of the hand samples (14 analyses), and b) using a micromill system at Institute of Earth Sciences Jaume Almera-CSIC (Barcelona, Spain) on a thick (300 microns) thin section of sample CAL 6 (22 analyses). The $\delta^{13}C$ and $\delta^{18}O$ values from these powdered samples were obtained in the Scientific and Technical Survey from Barcelona University (Spain). Samples were treated using 100% phosphoric acid at 70 °C. CO_2 was extracted using a Thermo Finnigan Carbonate Kiel Device III isotopic analyser with a Thermo Finnigan MAT-252 spectrometer incorporated, reproducing McCrea (1950) method. Values obtained were corrected using the standard NBS-19. Reproducibilities (2σ) (i) in hand samples are 0.04 for both stable isotopes, and (ii) for micromill samples are 0.04 ($\delta^{13}C$) and 0.1 ($\delta^{18}O$). The larger 2σ value for $\delta^{18}O$ of the micromill samples is probably due to the very low amount of sample analysed.

A wavelength dispersive electron probe microanalyser (WDS-EPMA), model JEOL JXA 8900 M at the ICTS-CNME Luis Brú of Complutense University of Madrid (Spain), was used to determine proportions and distribution of the main elements contained in the various laminae from a polished, and carbon-coated thin section of sample CAL-6. The microprobe was operated at an acceleration voltage of 15 kV, a probe current of 20 nA, and a spot size of 5 μm, with dwell times of 10 s (at peak positions) and 5 s (backgrounds).

Scan image of thin sections, and several microphotographs from sample CAL-6 were used to measure different lamina thicknesses using JMicrovision software (Nicolas Roduit) through an 8 mm long transect.

Temperature values (and also fractionation factors) were calculated using isotope fractionation equations for oxygen between calcite and water ($10^3 \ln\alpha_{cc\text{-}w}=17.4(10^3/T)-28.6$; Coplen, 2007), and for carbon between calcite and gaseous CO_2 ($10^3 \ln\alpha_{cc\text{-}CO_2}=11.98-0.12T$; Romanek et al., 1992). Calculations were done by assuming constant $\delta^{18}O_w$ and $\delta^{13}C_{CO_2(g)}$ values (Table 1) within the isotopic ranges for Gran Canaria compiled in literature of $\delta^{18}O_w$ from -2 to -6.5‰ SMOW, and $\delta^{13}C_{CO_2(g)}$ from-2 to -6‰ PDB (Gonfiantini et al., 1976; Albert et al., 1986; Custodio et al., 1987; Gasparini et al., 1990; Cabrera, 1995;).

The ranges of temperature obtained have been delimited by comparison with the range of groundwater temperatures commonly found in Gran Canaria of 15-35 °C (SPA-15, 1975; Gonfiantini et al., 1976; Custodio et al., 1987; Albert et al., 1986; Gasparini et al., 1990; Cabrera, 1995), by excluding the temperature series calculated which do not fall within the range reported.

DESCRIPTION OF THE CALABOZO CARBONATE DEPOSIT

General remarks

The Calabozo Carbonate Deposit is a relatively small build-up of less than 20 m long and about 10 m of maximum wide (Fig. 2A) composed of a suite of pools and cascade terraces fed from a broken irrigation system pipe (Fig. 2B). At present the build-up is dry; there is no flowing water. The deposit formed over the western wall of El Calabozo ravine, at 215 m asl. The water was sourced from wells situated 1.5-2.5 km to the SW of the Calabozo system, at about 450 m asl, with depths of up to 370 m. These groundwaters are bicarbonate-magnesium-rich, with

high CO_2 content, temperatures reaching 31 °C, with pH about 6 and electric conductivity ranging from 1500 to 2000 µS/cm (SPA-15, 1975; Alonso-Zarza et al., 2012).

It was not possible to obtain any written document on the activity of the irrigation system, but people from the nearby localities confirm that the irrigation system extended further south from the study area till the coast for the banana plantations. In northern Gran Canaria Island the activity of the banana plantations started in the nineteen fifties and ended by the nineties. The banana, an herbaceous plant with a vital cycle of more than one year, 20 to 24 months, requires humidity, but not prolonged periods of water saturation in the soil. Irrigation is done during 6 to 8 months per year, from spring to autumn, and during 2 to 4 days of every 10 to 20 days. During winter irrigation is generally stopped (Fernández Caldas & Fernández-Trujillo Martínez, 1962; Rodríguez Lupiañez, 1967; López Gómez, 1972).

The initial concrete irrigation pipe system, installed by 1950-1960, was later replaced by uralite® (towards 1970-1980) (Figure 2B). Carbonate deposition is related to the initial period when the outflow point of the pipe was situated at mid slope, from where the water flowed to reach the bottom of the Barranco. There are no carbonates above this exit point. The age of the build-up can additionally be deduced from the one coated clast fragment found with a nucleus of expandable polystyrene (EPS). EPS was patented Styropor® in 1950 (http://iwww.plasticsportal.com/products/styropor.html) by BASF company founded in Spain in 1966 (https://www.basf.com/documents/es/es/about-us/ES_Presentacion_centro_BASF_Tarragona.pdf). In short, very probably carbonate deposition started by the nineteen fifties and stopped around the eighties, indicating a maximum range of forty years for the formation of the Calabozo carbonate build-up.

Morphology

The carbonate build-up is composed of three main morphological elements (Fig. 3).

1) Relatively homogeneous slope (30-40 °) containing the exit of the original concrete pipe, with relatively continuous patches of yellowish carbonate composed of: a) thin, milimetric to centimetric, internally laminated carbonate crusts (Fig. 4A); b) powdery silty-micritic carbonate and c) Patches of coated stems, where the oncoid with the expandable polystyrene nucleus was found (Fig. 4B, C).

2) Pools of about 1 to 2 m in diameter, at present dry and with depth varying from 0.3 to 0.6 m (Fig. 4D), partially filled by debris of powdery carbonate, clays and vegetal fragments.

3) Cascade barriers, semicircular in shape and limiting (bounding) the pools (Fig. 4E, F), the more visible parts of the build-up, the main carbonate constructions. Some barriers coalesce into each other at the same elevation forming small terraces. Barriers develop from curtains (with small external rills) formed by the coalescence of hanging coated stems. Coated stems with thick coatings evolving into crusts appear in the lower and lateral parts of cascades. Accumulations of phytoclasts, either well preserved or their absence forming moldic porosity, appear together with crusts on top of barriers.

Mineralogy and facies types The mineralogy of the deposits is relatively homogeneous, being calcite the main component. Only one sample (CAL-5) contains minor amounts of clay minerals, quartz grains, fragments of volcanic rocks and Fe/Mn oxides/hydroxides. No aragonite was found.

Most textures observed in carbonate facies of El Calabozo deposit are micritic (Fig. 5A) or coarse crystalline (Fig. 5B). Micritic textures can be massive or laminated. Crystalline textures appear in the same facies as the micritic laminated textures.

Four main facies were recognized:

1. Framestones of coated stems are the most characteristic facies forming the cascade barriers (Figs. 4 E, F; and 5B). Textures of the coatings can be micritic laminated or coarse crystalline. Micritic laminated textures displays a dark-light coloured alternating lamination with wavy or crenulated morphologies. Coarse crystalline textures are composed of large, more than 300 µm long, columnar to branched-columnar to dendritic crystals, or crystal aggregates forming bands of the same thickness as the length of crystals (Figs. 5B-D). Such crystals/crystal aggregates contain alternating light-dark coloured lamination (Figs. 5B, C, E). More detailed description of the crystalline texture, its banding and laminated patterns, is provided in the lamination section below.

There are two main coated stem types, based on coating thickness: those with thin coatings of less than 600 µm, and those with thick coatings of several milimetres. The texture of thin coated stems is mainly but not exclusively, micritic laminated. The central ellipsoidal to

rounded pore is usually less than 1 cm in diameter (Fig. 5A). Microstructure of the encrusted plant part is preserved in the inner, first coating lamina. Organic filaments (Fig. 5F) and diatoms were commonly observed.

Thick coated stem texture present is mainly but not exclusively, crystalline. Mean diameter of coated stems is 4 cm; lengths range from 6 to 30 cm. Generally rounded to ellipsoidal central pores are usually about 1-8 mm in diameter. Thickness of coatings can increase vertically and/or laterally from progressively thicker coated stems into crusts or laminated bindstones, (described below). Although biogenic features are rare, calcified and non-calcified organic filaments and some broken diatoms were found (Fig. 5F).

2. Laminated bindstones form crusts in slopes and on top of barriers, commonly encrusting phytoclastic wackestones and thick-coated stems. Textures can be micritic laminated or crystalline (Fig. 6A), as those described for framestones of coated stems. Thickness of crusts is up to 0.3 mm, and individual laminae are generally less than 100 µm thick.

3. Phytoclastic wackestones are overlain by laminated bindstones in slopes and also on top of barriers. This facies consists of micrite which, in detail, is formed by very fine calcite crystals smaller than < 1 µm grouped into irregular spheroidal grains, containing leaves or other small plant parts (Fig. 6B). In particular, the most commonly observed type of phytoclast has spindle shaped morphology of about 1 mm long, and a hollow pentagonal morphology of about 300 µm in transversal section (Fig. 6C). Although phytoclasts are well preserved in general, some are partially or totally decomposed, having left moldic porosity.

4. Sandy mudstones filling pools consist of a poorly consolidated mix of micrite, and detrital material, including carbonate fragments (intraclasts), clays, clasts of volcanic rocks, and plant fragments (phytoclasts).

Lamination

Coarse crystalline textures, such as those of thick-coated stems or crusts (Fig. 5B), show laminated patterns consisting of bands of several hundreds of µm thick, composed of calcite crystal aggregates of the same length. Irregular micritic lamina, some containing detrital grains, may appear on top of a single crystalline band, that is on top of crystal aggregates.In

absence of such micritic lamina, crystals of the subsequent band start to grow directly on top of the previous band.

Crystal aggregates forming crystalline textures of El Calabozo deposit have cone-shaped overall morphology with the narrower part on the base and increasing width towards the top. In detail, three main typologies of cone-shaped crystal aggregates have been recognised: a) columnar (Fig. 7A, B), consisting of a non-branched cone; b) branched-columnar (Fig. 7C), similar to the previous type but developing some finger-like branching; and c) dendritic (Figs. 5C, 7D), consisting of several branches composed of stacked flat rhomb subcrystals of few μm in width.

Crystal aggregates contained in every single band also include alternating dark-light lamination showing crenulated morphologies, but some may have angular morphologies, depending on the type of crystal aggregate (Figs. 5B; 7B, C; 8). This lamination is best developed, or at least best preserved, in the outer bands, rather than in the inner (older) bands. This can be related to the larger size of calcite rhomb subcrystals coinciding with very thin intra-crystal aggregate discontinuities, which mostly occur in inner crystalline bands. EPS and preserved filaments appear commonly in outer bands (Fig. 5F), whereas nothing but moulds of the same characteristics as the filaments appear in inner bands. Some 50-100 μm thick laminated bindstones may occur intercalated with crystalline bands.

Thick calcified stem lamination is of a clearly crystalline laminated texture at five different scales observed both under optical and electronic microscope (the case of sample CAL-6 studied herein) (Fig. 8). Total thickness of the measured transect is about 8 mm, varying laterally between 6 and 12 mm. Lamination is visible due to the alternation of thick light coloured layers of coarse calcite crystal aggregates with thin darker coloured, some micrite, layers (Fig. 5B, E).

Five orders of lamination were recognised (Fig. 8). First order lamination ranges from 1.3 to 2.5 mm thick; second order from 0.5 to 0.9 mm thick; third order between 0.1 and 0.4mm thick; fourth order between 0.04 to 0.07 mm thick; and **fifth order** between 0.002 to 0.008 mm thick.

A forth order lamina is formed by 10-20 fifth order laminae; a third order lamina is formed by 4-6 forth order laminae; a second order lamina is formed by 2 third order laminae; and finally, a first order lamina is formed by 3 second order laminae (Fig. 8).

First and second, exceptionally third, order laminations are usually bounded by intercrystalline discontinuities bounding the end of crystal growth and beginning of new crystal, whereas the third to fifth order laminations are visible within crystals, therefore being intracrystalline discontinuities which represent stop-restart of crystal growth. In some cases, thickness of the different scale laminae overlaps, and in other cases the laminae are not well defined, as occurs mostly in the inner crystalline bands, probably due to early diagenesis. This can lead to mistakes in measurements.

Geochemistry

Isotope geochemistry

Stable isotopes of $\delta^{13}C$ and $\delta^{18}O$, were analysed from (a) whole rock samples collected all along the build-up, and (b) lamination of sample CAL-6.

- Values of $\delta^{13}C$ and $\delta^{18}O$ from samples collected all along the build-up: $\delta^{13}C$ ranges from +4.52 to +5.84‰ VPDB (mean=+5.40‰), while $\delta^{18}O$ ranges from -5.79 to -4.84‰ VPDB (mean= -5.20‰) (Fig. 9). However, the sample with the lowest $\delta^{13}C$ was the one containing trace amounts of quartz (sample CAL-5), not present in Gran Canaria rocks, but of aeolian origin. In consequence quartz may be accompanied by variable amounts of carbonate grains derived from marine limestones (Menéndez et al., 2007; Huerta et al., 2015). If this sample is excluded, the $\delta^{13}C$ range changes to +5.84 to +4.84 ‰ VPDB (mean= +5.47‰), whereas the range in $\delta^{18}O$ remains invariable. The regression line shows a positive trend, with R^2= 0.58 (excluding sample CAL-5).

The difference between the maximum and minimum values in both isotopes, $\mathbf{\Delta}\delta^{13}C$ and $\mathbf{\Delta}\delta^{18}O$ respectively, is of 0.97 ‰ for $\delta^{13}C$ and of 0.95 ‰ for $\delta^{18}O$ (excluding sample CAL-5). This coincidence in ranges should be taken into account in the discussion of the calculated values of temperature in next sections.

- Values $\delta^{13}C$ and $\delta^{18}O$ from lamination of sample CAL-6: $\delta^{13}C$ values range from +5.82 to +5.16 ‰ VPDB (mean= +5.44), and $\delta^{18}O$ values range from -4.6 to -6.1‰ VPDB (mean= -5.4‰). Mean $\delta^{13}C$ value of the lamination coincides with the value obtained from the CAL-6 whole rock analyses, whereas mean $\delta^{18}O$ value from lamination is 0.2‰ lower than the CAL-6 whole rock analyses. Regression line shows a positive trend, with R^2= 0.33

Isotope variation, $\Delta\delta^{13}C$ and $\Delta\delta^{18}O$, as was defined in the previous section, is respectively 0.66 and 1.5 ‰ that is, $\Delta\delta^{13}C$ is 2.3 times higher than $\Delta\delta^{18}O$. Both isotope values were plotted against distance or position of the sample, and both show positive trends in outward direction, that is, increasing values from older to younger laminae (Fig. 10).

Temperature, isotope fractionation and $\delta^{18}O_w$ and $\delta^{13}C_{CO_2(g)}$ calculations

The temperatures obtained by using both $\delta^{18}O$ and $\delta^{13}C$ fractionation equations independently are between 20 °C and 30 °C (Table 1). Temperatures and fractionation factors calculated for an individual series (i) at constant $\delta^{18}O_w$ show maximum temperature differences between the minimum and the maximum value of 7.7 °C, and about 1.5‰ for calcite-water oxygen fractionation factors; and (ii) at constant $\delta^{13}C_{CO_2(g)}$ the temperature differences between the minimum and the maximum value is 5.5 °C, and about 0.66 ‰ for calcite-gaseous CO_2 carbon fractionation factors (Fig. 10).

Elemental geochemistry

EMP analyses (Table 2) show that Ca is the main element present in the calcite found in the lamina (53-56 wt. %), followed by Mg (0.5-2 wt. %). Mn (0-3000 ppm), Fe (0-1500 ppm), Sr (0-800 ppm) and Al (0-600 ppm), all of which appear in variable amounts. Si only appears exceptionally. These proportions, expressed as mole % of carbonates of different elements, were compared (Fig. 11). The most relevant is $MgCO_3$-$CaCO_3$ (negative and with R^2= 0.98). Interesting are the negative relationships $MgCO_3$+$SrCO_3$-$MnCO_3$+$FeCO_3$, (R^2= 0.41), $MgCO_3$-$MnCO_3$ (R^2= 0.27), and the positive $MnCO_3$+$FeCO_3$-$CaCO_3$ relationship (R^2=0.29). No correlation was found between Al and the other elements analysed.

Electron microprobe elemental maps (Fig. 12) show very low Fe content, dispersed over broad bands. Mn, Mg and Ca appear clearly related to lamination. Laminae of 4th order have couplets of thick Ca-Mn rich layer at their base, passing to a thin Mg-rich layer at their top. Laminae of 3rd order present two opposite patterns; (i) increasing Mn-decreasing Mg from base to top, and (ii) the vice versa. Finally, 2nd order lamination exhibits generally trending increase in Mg and decrease in Mn from base to top. Ca variations are clear only at a scale of 4th order

lamination. In addition, in some areas, the Ca, Fe and Mn distributions do not seem to follow any clear trend.

INTERPRETATION AND DISCUSSION

Formation of the carbonate build-up

Morphologically El Calabozo deposit can be classified as an inactive barrage system developed on a slope (Pentecost and Viles, 1994), forming a terraced slope build-up (Guo and Riding, 1998; Pedley, 2009; Della Porta, 2015) which consists of a succession of cascade-barriers and subsequent pools.

Barriers, cascades and pools typically develop in spring (e.g. perched) and fluvial (meteogene) tufa systems, but here the barriers and cascades consist of bryophyte boundstones-framestones and/or stromatolites (Pedley 1990; Carthew et al., 2003; Ordoñez et al., 2005; Vázquez-Urbez et al., 2012). In the case of El Calabozo deposit, macrophyte stems creating small obstacles were subsequently coated by coarse crystalline calcite. Their coarse (dendritic) crystals probably reflect rapid precipitation under disequilibrium conditions (Jones and Renaut, 2010) caused by outgassing of dissolved CO_2 after its outflow from the pipe, probably also helped by the turbulence of high flow velocity (as in “dense travertine” of Okumura et al., 2012) due to the slope gradient. Even so, facies from El Calabozo deposit are those typically described in tufa deposits (Arenas-Abad et al., 2010). In consequence, macrophytes played a major role in the formation of the build-up.

The intercalations of thin micritic laminae indicate slow flows or even drying of the system, allowing the development and preservation of some microbial communities which induce both micrite precipitation and/or micritization of external parts of coarse crystals (Camuera et al., 2014; Alonso-Zarza and Rygaloff, 2017). Coalescence of stems indicates the uninterrupted water flow across the barriers, favouring thickening of coatings.

Lamination as related to irrigation system water supply.

Laminated calcite or aragonite deposits, have been typically reported from caves (Baker et al., 2008; Romanov et al., 2008;), but also from tufa (Matsuoka et al., 2001; Kano et al., 2003; Kawai et al., 2009), and travertines (Okumura et al., 2011; 2012; 2013a, b), among others.

In the case of speleothems, these laminated facies show differences in petrology, mineralogy, trace elements, stable isotopes, organic matter (Roberts et al., 1998; Dasgupta et al., 2010; Fairchild and Baker, 2012; Muñoz et al., 2015). These laminae, occurring at different timescales, are annual in some regions with significant annual variations in processes that affect formation (Genty et al., 1997; Tan et al., 2006), such as dripping rates, chemistry of cave waters, fluctuations of the cave atmosphere, affecting CO_2 concentration, humidity or air flow. Sub-annual and super-annual laminae occur as well, but have been less frequently reported (Baker et al., 1999; Baker et al., 2008).

Tufa deposits generally exhibit biannual lamination, alternating between porous (e.g. rainy season) and dense (e.g. dry season) laminae, reflecting seasonal changes in precipitation rates of calcite (Matsuoka et al., 2001; Kano et al., 2003; Kawai et al., 2009). Such changes are generally due to dilution of waters during the rainy season, decreasing the precipitation rate of calcite as well as the saturation index, whereas waters contain higher concentrations during the dry season, when precipitation rates increase (Matsuoka et al., 2001; Kano et al., 2003; Kawai et al., 2009). However, these seasonal changes may differ, depending on the climate setting and related hydrological conditions of the tufa depositing area (Kano et al., 2003), and may not be evident from waters containing more than 65 mg/l of Ca (Kawai et al., 2009).

Travertine lamination has been reported as seasonal, with thicknesses of 0.1 to more than 10 mm, due to variation in parameters controlling $CaCO_3$ precipitation rate, as in the case of tufa (Kano et al., 2003; Liu et al., 2006; 2010). Daily lamination of 100-500 µm thick has been reported too, suggesting their potential as high resolution palaeoclimatic archives (Okumura et al., 2011, 2012, 2013a, b). However, it has been found that formation of daily lamina is controlled by microbial inhibition/promotion of inorganic $CaCO_3$ precipitation during the day, and by inorganic precipitation during the night (Okumura et al., 2013a, b). The extent of microbial influence during daytime deposition seems to be controlled by flow velocity, which controls the thickness and development of microbial biofilms on surface, and by the calcite (or aragonite) precipitation rate (Okumura et al., 2013b).

General controls of formation of all these systems and of their changes throughout the year are mostly climate-related. In fact, interpretations from stable isotope records from active

travertine sites have been stated in terms of rainfall amounts and other seasonal changes (Liu et al., 2006). However, while active systems can be studied throughout the year, fossil systems/deposits cannot. Such deposits require petrological analyses. Unlike naturally occurring systems, El Calabozo deposit was totally human managed. In consequence, some particular considerations are pointed out in the following:

- Seasonal and daily patterns, if present, were not recorded as a textural change (e.g. porous-dense), as in the case of naturally-working systems. In El Calabozo, the most common seasonal and daily pattern observed is a couplet of crystalline lamina-discontinuity, instead of changes from dense to porous laminae, common in most natural systems (Kano et al., 2003; Kawai et al., 2009)

- El Calabozo system flowed discontinuously; therefore precipitation, occurring during short periods, was followed by longer periods of interrupted sedimentation, at all timescales considered. In consequence, thicknesses of seasonal and daily lamina, if observed, should be thinner than those reported from travertines (Okumura et al., 2013a, b).

Therefore, crystal growth only could occur during the short times of water flow, that is, for a few hours per day. In consequence, the smaller, fifth order lamination might be a result of the daily short period irrigation. Since each fourth order lamina contains 10-20 5^{th} order laminae, the time needed to form a forth order lamina would be on the order of 10 to 20 days, which fits very well with reported irrigation cycles (Fernández Caldas & Fernández-Trujillo Martínez, 1962). Third order laminae, composed of 4-6 4^{th} order laminae would take 40 to 120 days to form, or 1 to 4 months. A second order lamina would need up to 240 days, or 8 months. As irrigation was done mostly between spring and autumn, during about 8 months, and the system was (almost) idle during winter (Fernández Caldas & Fernández-Trujillo Martínez, 1962; Rodríguez Lupiañez, 1967; Lopez Gomez, 1972) a 2^{nd} order lamina would be formed over 8 months at least. Then its annual bounding discontinuity may represent winter interruption that is 4 months. In consequence, 3^{rd} order laminae represent 4 months formation and may be related to seasonal variation of irrigation frequency. First order lamination may represent three year periods, composed of three 2^{nd} order (annual) laminae. Laminae of 1^{st} order may be related to downtime of the pipe system, after which it was repaired for the first time, which corresponded to the end of formation of the build-up. Irrigation was not continuous on any scale of time, so such times are reflected in the formation of the crystalline laminae and in their bounding discontinuities. Estimations of the average deposition rates of the 8 mm transect of sample CAL-6 were done. Assuming that 0.5-0.9 mm thick 2^{nd} order laminae is very

probably annual, then the 8 mm transect may represent 8.9-16 years. However different precipitation rates ranging between 0.7 and 2.9 mm/year were obtained by considering 3rd to 5th order laminae. This suggests the lower the time span considered the higher the calculated precipitation rate, as a consequence of the short duration of effective precipitation ~~time spans~~ due to the long interruption periods. Considering 2-8 μm thick lamina is not daily but produced in few hours, around 4-8 hours periods, calcite precipitation rates may range between 4.4 and 17.5 mm/year, and 2.2 and 8.8 mm/year respectively.

The lower precipitation rates fit very well with reported seasonal precipitation rates for tufa laminations (Matsuoka et al., 2001; Kano et al., 2003; Arenas and Jones, 2017). The higher precipitation rates fit well with reported seasonal precipitation rates for travertine laminations (Liu et al., 2006; 2010), but they are lower than those reported from daily travertine lamination (Okumura et al., 2011; 2012, 2013a, b)

The discrepancies, low precipitation rates at longer scale times and *vice versa*, is a reflection of the highly erratic water supply and resulting crystal growth in El Calabozo system. Accuracy of estimation of precipitation rates strongly depends on estimation of the duration of interruption in sedimentation.

Geochemistry and calcite precipitation

Geochemical variations seem to be related to 2nd, 3rd, and 4th order laminations. Annual decrease of Mn and increase of Mg from base to top in 2nd order laminae may be due to increasing irrigation frequency from spring to summer-autumn, as ambient temperature increased. The two 3rd order laminae included in 2nd order ones show opposite trends: (i) increasing Mn-decreasing Mg, with laminae increasing their thickness upwards (spring) and (ii) increasing Mg-decreasing Mn (summer-autumn), both from base to top. This may account for an increase in number of days per irrigation from 2 to 4 days every irrigation cycle, and an increase in the frequency of irrigation during summer from irrigation every 20 days to irrigation every 10 days.

Laminae of 4th order, related to irrigation cycle of 10 to 20 days display geochemical couplets consisting of a thick basal lamina with relatively high Ca and Mn (+Fe), and relatively low Mg contents, followed by a thin lamina on top with relatively high content of Mg, lower content of Ca and absence of Mn (+Fe). Coupled variations between Ca-Mn(+Fe) and Mg fit well with the expected behaviour of those elements based on their calcite and water partition coefficients.

Mn and Fe partition coefficient values greater than one under equilibrium conditions are preferentially incorporated into the calcite structure (Rimstidt et al., 1998). Therefore, thick laminae rich in Ca-Mn / poor in Mg may have precipitated under conditions trending to chemical equilibrium. The thin laminae at the top of 4^{th} order laminae are enriched in Mg, poor in Ca-Mn, where Mn disappears, Ca decreases and Mg increases, suggesting precipitation under more disequilibrium conditions than those prevalent for the previous thick lamina. Greater amounts of elements with equilibrium partition coefficient values smaller than one tend to enter in higher proportions into the calcite structure and those with equilibrium partition coefficients greater than one tend to enter in lower proportions (Rimstidt et al., 1998). The end of the precipitation of 4^{th} order laminae is related to the interruption of irrigation and drying of the system. An increase in evaporation leading to chemical disequilibrium may explain the increasing Mg content on top of 4^{th} order laminae concurring with a discontinuity in sedimentation (Rimstidt et al., 1998). Such desiccation may involve the decay of the microbial community and the degradation of biofilm and EPS, matching with the higher Mg content. This is apparently opposite to that described by Saunders et al. (2014), where biofilm acts as an ionic sieve producing low Mg contents within the biofilm and in the calcite precipitated in it. The presence of Mg in all analysed samples may also suggest a relatively high Mg/Ca ratio in waters from which calcite precipitated in El Calabozo deposit.

Isotope trends, disequilibrium and water temperatures

Both stable isotopes from deposit samples display similar ranges, an outstanding feature, because $\delta^{13}C$ isotope fractionation involves many processes and complex relationships (Myrttinen et al., 2015). This suggests both $\delta^{13}C$ and $\delta^{18}O$ values of calcite were produced under disequilibrium conditions. Ranges of values from both stable isotopes are narrower than those reported from caves, tufas and travertines (Mickler et al., 2004; Liu et al., 2006, 2010; Kawai et al., 2009; Kele et al., 2011; Okumura et al., 2011, 2012; Hansen et al., 2013; Dreybrodt and Romanov, 2016). In all these environments stable isotopes usually show seasonal variations related to factors controlling calcite precipitation (Kano et al., 2003; Kawai et al., 2009; Liu et al., 2010) which may be reflected in a different manner or not reflected in El Calabozo deposit. This can explain the low isotope ranges in El Calabozo, compared to those reported in literature from natural systems.

Values of $\delta^{13}C$-$\delta^{18}O$ show a positive covariant trend, similar to that typically reported from calcite-precipitating systems with strong CO_2 degassing, although such a trend is less clear in El Calabozo (r^2= 0.58) than in active systems (Kele et al., 2011).

Degassing of CO_2 and calcite precipitation has been found to occur in the following three steps in caves, and under laminar water flow (Hansen et al., 2013): (1) CO_2 degassing occurs without change in pH and Ca^{2+} content; (2) re-equilibration of DIC species to the new (lower) pCO_2 with increase of pH; and (3) calcite precipitation with slight pH decrease. The time needed for CO_2 degassing is 10 times lower than the time required for attaining chemical equilibrium between DIC species, and 100 times lower than the time needed for calcite precipitation (Hansen et al., 2013). In addition, turbulence, a common feature of flowing waters at travertine- and tufa-depositing sites, may contribute strongly to sudden mechanical CO_2 degassing, as occurs in fast flowing waters, related to vertical steps (Zhang et al., 2001). Therefore, the time needed for CO_2 degassing should be quite short, and then chemical re-equilibrium occurred among DIC species, and calcite precipitated, being the latter obvious, as calcite precipitation is observed. In consequence, the whole three steps process should be very fast.

Waters forming El Calabozo deposit would have pH values around 7 (SPA-15, 1975; Gasparini et al., 1990), therefore with HCO_3^- the dominant DIC specie. In consequence, during chemical re-balancing after CO_2 degassing, CO_2 formed from HCO_3^-, along with calcite from bicarbonate in the subsequent third step.

On the other hand, there is not a clear proximal to distal $\delta^{13}C$ trend increase, which would be directly attributable to CO_2 degassing plus $CaCO_3$ precipitation. Such a lack of trend could be the consequence of sudden and repeated CO_2 degassing inhibiting isotope equilibrium. Although chemical equilibrium is a necessary condition to achieve isotopic equilibrium, the latter may not be achieved even though chemical equilibrium has been reached. For example, DIC species may chemically and isotopically re-equilibrate between them, but not yet isotopically re-equilibrate with H_2O due to the different velocities of the reactions involved (Dreybrodt et al., 1996; Ferronsky and Polyakov, 2012). This lack of isotope equilibrium (independent of chemical equilibrium) could imply that the newly formed CO_2 and precipitated calcite would have low, non-equilibrium isotope fractionations both referred to HCO_3^-. The short length and stepped longitudinal profile of the build-up, together with inferred flow velocities > 0.7 m/s (according to Okumura et al., 2012), could have impeded isotopic equilibrium between DIC species, as mechanical degassing occurred repeatedly in short distances as the waters flowed. The fact that both stable isotopes vary within the same range, and generally with the same trend, may also suggest there was not re-balancing between DIC and water as a consequence of relatively long duration of such re-equilibrium (Beck et al.,

2005; Romanov et al., 2008). However, CO_2 degassing leading to calcite precipitation is only one of the many different kinetic processes affecting isotope fractionation.

Other process causing kinetic effects on isotope fractionation is high rates of $CaCO_3$ precipitation. Precipitation rates of calcite found in the previous section are high, and comparable to those of tufas and even travertines (Kano et al., 2003; Okumura et al., 2013a, b). The effect of such high precipitation rates, or fast calcite precipitation, causes stable isotope signals of calcite to tend towards those of bicarbonate, that is, calcite-HCO_3^- isotope fractionation tends towards zero (Mickler et al., 2004; Kele et al., 2011).

In summary, calcite isotope signals would be similar to those of HCO_3^-, and both their stable isotopes vary slightly and in the same way, probably due to the lack of chemical equilibrium between DIC and water, and the lack of isotope equilibrium in CO_2-HCO_3^-, and $CaCO_3$-HCO_3^- pairs.

Disequilibrium (isotopic and/or chemical), the dominant condition in this kind of system, is a delicate issue for isotope-based temperature calculations. $CaCO_3$ precipitation, CO_2 degassing and other important processes occurring in such natural systems cause disequilibrium and kinetic processes affecting the isotopic signal (Kele et al., 2011; Nielsen et al., 2012).

Temperatures calculated using carbon isotope fractionation equations are not reliable in general, because of the high degree of uncertainty involved (Myrttinnen et al., 2012). However, calculations using ^{13}C fractionation equations provided interesting results in this case, as they are comparable to those obtained by using ^{18}O fractionation equations, which deserve attention.

On the other hand, isotope-based temperature calculations require isotopic equilibrium. In consequence, such temperature calculations would not be feasible, at least in small systems with fast flowing waters, where isotopic equilibrium is not attained; unlike in larger systems, in which isotopic equilibrium tends to be reached distally to the outflow point (Kele et al., 2011).

However, temperature calculations using $\delta^{18}O$ from carbonates at the outflow point have been made successfully, despite conditions of chemical and isotopic disequilibrium, as precipitated $CaCO_3$ possesses an isotopic signal equal to, or close to that of HCO_3^- (Kele et al., 2008; 2011). Moreover, these authors assumed there is not $CaCO_3$ precipitation before water reaches the outflow point. Such assumption seems to be unfounded, as $CaCO_3$ precipitates underground, for example on walls from fractures serving as conduits for water movement (Gratier et al., 2012; Rodríguez-Berriguete et al., 2017). In any case, calculations proposed by Kele et al. (2008 and 2011) actually work, as they are based on the hypothesis by O'Neil et al. (1969) of absence of isotopic fractionation during fast calcite precipitation, the result of very fast CO_2 degassing.

The Coplen (2007) equation fits very well with the "non-equilibrium empirical travertine curve" (Kele et al., 2011) at the low temperature range. In fact, The Coplen (2007) equation provides higher calcite-water isotope fractionations than those from experiments and calculations (Friedman & O'Neil, 1977; Kim & O'Neil, 1997; Chacko & Deines, 2008). In consequence, The Coplen equation has been regarded as a non-equilibrium equation, therefore considered invalid for temperature calculations. Whereas experiments by Dietzel et al. (2009), as well as results from clumped isotopes (Kluge et al., 2014) supported Coplen results, but involves the assumption that this equation includes kinetic isotope effects common in natural systems, which cannot be eliminated (Dietzel et al., 2009).

Under these assumptions, isotope-based temperatures can be calculated using the Coplen (2007) equation, as isotopic and chemical conditions at El Calabozo fit very well with those reported from many other natural systems (Coplen, 2007; Dietzel et al., 2009; Kele et al., 2011; Yan et al., 2012), as has been discussed above.

Stable isotopes, both $\delta^{13}C$ and $\delta^{18}O$, from a laminated sample, display positive trends, that is increasing values from base to top. These data have been taken from the lamination of a sample representing sedimentation throughout time at a fixed point. Both increasing base to top trend, or throughout time trend, could be related to climate changes affecting groundwaters, such as changes in rainfall amount, or in-soil CO_2, among many others (Kano et al., 2003; Mickler et al., 2004; Liu et al., 2006, 2010). On the other hand, the range of $\delta^{18}O$ is 2.3 times larger than the range of $\delta^{13}C$. This difference between both stable isotope ranges is compatible with temperature-controlled isotope fractionations, according to equations $10^3 ln\alpha_{cc\text{-}CO_2}$=11.98-0.12T (Romanek et al., 1992) and $10^3 ln\alpha_{cc\text{-}w}$=17.4($10^3$/T)-28.6 (Coplen, 2007). Each independently provided temperatures in similar ranges. This is unusual, as $\delta^{13}C$-based calculations do not provide reliable temperatures in general. However, the variations or ranges in temperature independently provided by each stable isotope are about 6-8 °C, which is not within the expected change in groundwater temperatures of the area, for the time lapse considered (SPA-15, 1975). Moreover, small variations in $\delta^{13}C_{DIC}$ and $\delta^{18}O_w$ are expected, as none of them have been reported from groundwaters of Gran Canaria (SPA-15, 1975; Gonfiantini et al., 1976; Gasparini et al., 1990). Therefore, if strong changes, such as those calculated, in Tw, $\delta^{13}C_{DIC}$ and $\delta^{18}O_w$ are not expected, then what caused the increasing base to top trend in both stable isotopes in the same fixed point of the build-up?

Assuming the same water velocities throughout the entire history of sedimentation, as the system was managed and the same flow rate could be expected, then changes in calcite signal throughout time should be due to (a) increase in calcite-water isotope fractionation

throughout time; or (b) changes in path length and/or residence time of waters as the build-up grew. The former option is not possible in our opinion as systematic changes in isotope fractionation may be generally related to changes in water temperature (Kim & O'Neil, 1997), which are not expected within large ranges, as explained before. The latter option has been reported for cave systems; as the path followed by waters increases, waters reaching the same point are progressively more degassed (Mickler et al., 2004; Mülinghaus et al., 2009; Deininger et al., 2012). However, calcite crusts from Roman aqueducts do not show any increasing trend in their stable isotope record, reflecting just environmental-related changes (Sürmelihindi et al., 2013; Passchier et al., 2016). These aqueduct crusts show only vertical growth within the aqueduct (Sürmelihindi et al., 2013), possibly representing an aggradational pattern. The simplest way to increase the length of the path followed by water and/or the residence time in spring-related systems is the progradation (± aggradation) of the build-up. In consequence, the increasing base to top trend in both stable isotopes would not be a climate-related feature, and for this reason, corrections leaving mean calculated temperatures unchanged were applied in order to eliminate the effect of build-up growth, assuming the change occurred throughout time is due to the progressive growth of the build-up.

A correction was made to the regression lines of calculated temperatures (T_w) plotted against distance (Table 1; Fig. 10), in order to eliminate the effect of the slope of the increasing outwards trend of isotope values, by assuming such regression line slope could be due to parameters other than temperature.

For this correction, the series with a mean temperature value coinciding with the median of the calculated temperature range ($T_{w\ mean}$) were chosen. These temperatures are close to 25 °C, using both $\delta^{13}C$ and $\delta^{18}O$ fractionation equations (24.7 °C for oxygen and 25.3 °C for carbon derived temperatures). Regression line equations in the form T=a*Distance-b were obtained (being a the slope of the line, and b the intercept of the line to Y axis), and used to calculate corrected temperature values ($T_{w\ corr}$) in the form $T_{w\ corr}=T_w-(a*Distance-b-T_{w\ mean})$. The same was done for fractionation factors (Table 1). The corrected temperatures and fractionation factors yielded slightly decreased ranges (here as the difference between the maximum and the minimum value) of 6.1 °C and 1.2 ‰ for oxygen, and 4.9 °C and 0.6 ‰ for carbon, without any change in the mean values of both series (Fig. 10).

The long time scale trends of isotope signals and then the range of calculated temperatures diminished once our correction was applied. Therefore, growth of a build-up should be considered before that of climate effects on interpretation of stable isotope signals from laminated carbonates.

Different kinetic or disequilibrium effects may act over different time scales and with different magnitudes, introducing some kind of noise to both the isotopic signal and to the calculated temperatures. In consequence, uncertainties may increase due to the higher probability of measured isotopic signals affected by kinetic effects during crystal growth under high precipitation rates (Nielsen et al., 2012).

To summarise, the isotope data throughout the entire lamination from laminated sample fit very well in general terms with temperature changes. However, some isotope effects counterbalancing opposing trends in $\delta^{13}C$ and $\delta^{18}O$ may introduce errors in the temperatures calculated over different time scales that should be considered when interpreting palaeoclimatic signals in this type of deposit. Our study focussed on a relatively recent deposit, formed during second half of the 20^{th} century, but even so, obtaining palaeoclimate information from it was difficult. Greater difficulties can be expected in older deposits, due to greater uncertainties in water isotope signals and longer time periods allowing diagenetic changes. In order to extract reliable information from this type of deposit, combined petrological, geochemical and isotopic analyses should be required.

CONCLUSIONS

This study describes a small human-induced stepped tufa deposit, formed mainly by a succession of cascade-barriers and pools, consisting of framestones of coated stems, laminated bindstones, phytoclastic wackestones and silty mudstones. Framestones and bindstones display micritic or coarse crystalline laminated textures.

Lamination from a sample with coarse crystalline texture show 5 orders of magnitude, from daily to annual or longer, according to irrigation cycles of banana plantations in Gran Canaria volcanic island. Precipitation rates were al least of 0.7 mm/year, or higher if discontinuity at all time scales is considered. Coarse crystalline textures are very commonly found, and attributed to high precipitation rates under relatively high flow velocities. Elemental geochemistry suggests incorporation of cations under, or close to equilibrium chemical conditions, except when the system flow was interrupted and Mg^{2+} concentration increased as a consequence of evaporation and degradation of microbial products. However, stable isotopes indicate chemical and/or isotopic disequilibrium during calcite precipitation.

Despite such isotopic disequilibrium, temperature calculations are possible in the absence of isotope fractionation of calcite and CO_2 referred to HCO_3^-. The effect of progradation of build-up on both stable isotope signals through lamination was corrected, providing a more accurate

temperature range, with a mean value of 25 °C. The same temperatures were obtained by using each stable isotope independently. Thus it seems that in this relatively recent system, accuracy is increased by taking into account large temporal scales. Palaeotemperatures obtained from the isotopic values of individual lamina may reflect small scale physical, chemical and biological processes.

In short, this study based on a human-induced short-lived tufa system, illustrates the mechanisms that cause different scales of lamination, variable rate of precipitation due to the discontinuous water flow, petrological and geochemical differences between the laminae and their causes. Only with all the other data, would it be possible to obtain reliable palaeotemperature estimations in similar deposits.

ACKNOWLEDGEMENTS

This work was funded by projects CGL2014-54818-P from the Spanish Ministerio de Ciencia e Innovación. J. Cerne reviewed the English version of the manuscript. Special thanks to A. Meléndez and F.J. Pérez-Torrado for field assistance. Dr. Pufahl, J. Dabkowski, G. DellaPorta and an anonymous reviewer greatly helped to improve the original manuscript.

REFERENCES

Albert, J.F.; Araña, V., Diez, J.L.; Filly, A. and **Fontes, J.Ch**. (1986) Modelo termodinámico de la actividad del Teide. *Anal. Fis.*, Serie B, especial, **82**, 86-201.

Alonso-Zarza, A. M., Rodríguez-Berriguete, A., Cabrera, M. C., Meléndez, A., and **Martín-Rodríguez, L. F.** (2012). Las tobas/travertinos del Barranco de Calabozo: un ejemplo de construcción rápida de un edificio carbonático alimentado por una tubería de regadío. *Geotemas*, **13**, 44-47.

Alonso-Zarza, A. M., and **Rygaloff, A.** (2017). Fluvial carbonate occurrences in high energy rivers: Examples from the Gállego River Tributaries, Pyrenees, Huesca. *Geogaceta*, **61**, 151-154.

Andrews, J. E., Riding, R., and **Dennis, P. F.** (1997). The stable isotope record of environmental and climatic signals in modern terrestrial microbial carbonates from Europe.*Palaeogeography, Palaeoclimatology, Palaeoecology*, **129**(1-2), 171-189.

Arenas-Abad, C., Vázquez-Urbez, M., Pardo-Tirapu, G., and **Sancho-Marcén, C.** (2010). Chapter 3: Fluvial and Associated Carbonate Deposits. In: *Carbonates in continental settings: Facies, environments and processes* (Eds. A.M. Alonso-Zarza and L.H. Tanner). Developments in Sedimentology 61, pp. 133-175.

Arenas, C., & **Jones, B.** (2017). Temporal and environmental significance of microbial lamination: Insights from Recent fluvial stromatolites in the River Piedra, Spain. *Sedimentology*, **64**(6), 1597-1629.

Baker, A., Fuller, L., Genty, D., Fairchild, I.J., Jex, C. and **Smith, C.L.** (2008). Anually laminated speleothems: a review. *International Journal of Speleology*, **37**, 193-206.

Baker, A., Proctor, C.J., Barnes, W.L. (1999). Variations in stalagmite luminescence laminae structure at Poole's Cavern, England, AD 1910 to AD 1996: calibration of a palaeoprecipitation proxy. *The Holocene*, **9**, pp 683-688

Barton, L. (2005). *Structural and Functional Relationships in Prokaryotes*. Springer Science & Business Media, 817 pp.

Beck, W.C., Grossman, E.L., and **Morse, J.W.** (2005) Experimental studies of oxygen isotope fractionation in the carbonic acid system at 15°, 25°, and 40°C. *Geochimica et Cosmochimica Acta*, **69**, 3493-3503.

Cabrera, M.C. (1995) Caracterización y funcionamiento hidrogeológico del acuífero costero de Telde (Gran Canaria). PhD Thesis. Salamanca University. 388 pp

Camuera, J., Alonso-Zarza, A.M., Rodríguez-Berriguete, A., and **Rodríguez-González, A.** (2014) Origin and palaeo-environmental significance of the Berrazales carbonate spring deposit, North of Gran Canaria Island, Spain. *Sedimentary Geology*, **308**, 32-43.

Capezzuoli, E., Gandin, A., and **Pedley,M.** (2014) Decoding tufa and travertine (fresh water carbonates) in the sedimentary record: the state of the art. *Sedimentology*, **61**, 1–21.

Carthew, K.D., Taylor, M.P., and **Drysdale, R.N.** (2003) Are current models of tufa sedimentary environments applicable to tropical systems? A case study from the Gregory River. *Sedimentary Geology*, **162**, 199-218.

Chacko, T., and **Deines, P.** (2008). Theoretical calculation of oxygen isotope fractionation factors in carbonate systems. *Geochimica et Cosmochimica Acta*, **72**(15), 3642-3660.

Chafetz, H.S. and **Guidry, S.A.** (1999) Bacterial shrubs, crystal shrubs, and ray-crystal shrubs: bacterial vs. abiotic precipitation. *Sedimentary Geology*, **126**, 57-74.

Chafetz, H., and **Lawrence, J.** (1994). Stable isotopic variability within modern travertines. *Géographie physique et Quaternaire*, **48**(3), 257-273.

Coplen, T.B. (2007) Calibration of the calcite-water oxygen-isotope geothermometer at Devils Hole, Nevada, a natural laboratory. *Geochimica et Cosmochimica Acta*, **71**, 3948-3957.

Custodio, E., Hoppe, J., Hoyos-Limón, A., Jiménez, J., Plata, A., and **Udluft, P.** (1987) Aportaciones al conocimiento geohidrológico de Tenerife utilizando isótopos ambientales. IV Simposio de Hidrogeología, Palma de Mallorca, Spain.

Custodio, E. (1985): Low permeability volcanics in the Canary Islands (Spain). In: *Hydrogeology of rocks of low permeability*. International Association of Hydrogeologists, Tucson, Ariz., pp 533–544.

Custodio, E. and **Cabrera, M.C.** (2008): Synthesis of the Canary Islands hydrogeology. In: *International symposium in Hydrogeology-Hydrogeology of volcanic rocks*, 51-56.

Custodio, E. and **Cabrera, M.C.** (2013): The Canary Islands. In: *Water, Agriculture and the Environment in Spain: can we square the circle?* (Eds. L. Di Estefano and M.R. Llamas). CRC Press/Balkema, 281-289

Dasgupta, S., Saar, M.O., Edwards, R.L., Shen, C.C, Cheng, H., and **Alexander, E.C.** (2010) Three thousand years of extreme rainfall events recorded in stalagmites from Spring Valley Caverns, Minnesota. *Earth and Planetary Science Letters*, **300**, 46-54

Deininger, M., Fohlmeister, J., Scholz, D. and **Mangini, A.** (2012) Isotope disequilibrium effects: The influence of evaporation and ventilation effects on the carbon and oxygen isotope composition of speleothems-A model approach. *Geochimica et Cosmochimica Acta*, **96**, 57-79.

Della Porta, G. (2015). Carbonate build-ups in lacustrine, hydrothermal and fluvial settings: comparing depositional geometry, fabric types and geochemical signature. *Geological Society of London Special Publications*, **418**, 17-68.

Dietzel, M., Tang, J., Leis, A., and **Köhler, S. J.** (2009). Oxygen isotopic fractionation during inorganic calcite precipitation—Effects of temperature, precipitation rate and pH. *Chemical Geology*, **268**(1), 107-115.

Dreybrodt, W., and **Romanov, D.** (2016). The evolution of ^{13}C and ^{18}O isotope composition of DIC in a calcite depositing film of water with isotope exchange between the DIC and a CO_2 containing atmosphere, and simultaneous evaporation of the water. Implication to climate proxies from stalagmites: a theoretical model. *Geochimica et Cosmochimica Acta*, **195**, 323-338.

Dreybrodt, W., Lauckner, J., Zaihua, L., Svensson, U., and **Buhmann, D.** (1996). The kinetics of the reaction $CO_2 + H_2O \rightarrow H^+ + HCO_3^-$ as one of the rate limiting steps for the dissolution of calcite in the system H_2O-CO_2-$CaCO_3$. *Geochimica et Cosmochimica Acta*, **60**(18), 3375-3381.

Eiler, J. M. (2011). Paleoclimate reconstruction using carbonate clumped isotope thermometry. *Quaternary Science Reviews*, **30**(25), 3575-3588.

Estrella de Pinho, R.R., Rodríguez-Berriguete, A., Alonso-Zarza, A.M., and **Cabrera, M.C.** (2015) The Temisas Carbonate Building: an example of a thermogene tufa system in Gran Canaria Island. *Geogaceta*, **57**, 7-10.

Fairchild, I., Baker, A. (2012) Speleothem Science: From Process to Past Environments. Wiley-Blackwell, Oxford. 450pp.

Fernández Caldas, E. and **Fernández-Trujillo Martínez, F.** (1962) Plátanos, fertilización y técnicas de cultivo en Canarias. *Actas de la I Reunión Plenaria del Instituto de Edafología y Agrobiología del CSIC*, **5**, 353-372. Salamanca, Spain.

Ferronsky, V. I., and **Polyakov, V. A.** (2012). *Isotopes of the Earth's Hydrosphere*. Springer Science & Business Media, 628 pp.

Friedman, I., and **O'Neil, J. R.** (1977). *Data of geochemistry: Compilation of stable isotope fractionation factors of geochemical interest* (Vol. 440). US Government Printing Office.

Gandin, A. and **Capezzuoli, E.** (2014) Travertine: distinctive depositional fabrics of carbonates from thermal spring systems. *Sedimentology*, **61**, 264–290.

Gasparini, A., Custodio, E., Fontes, J.C., Jimenez, J., and **Nuñez, J.A.** (1990) Exemple d'etude geochimique et isotopique de circulations aquiferes en terrain volcanique sous climat semi-aride (Amurga, Gran Canaria, Iles Canaries). *Journal of Hydrology*, **114**, 61-91.

Genty, D., Baker, A., and **Barnes W.L.** (1997) Comparison of annual luminescent and visible laminae in stalagmites. Comptes Rendus Academie Sciences Paris, Serie II, **325**, 193-200

Gonfiantini, R., Gallo, G., Payne, B.R., and **Taylor, C.B.** (1976) Environmental isotopes and hydrochemistry in groundwater of Gran Canaria. In: *Interpretation of Environmental Isotope and Hydrochemical Data in Groundwater Hydrology* (Ed. Staff, I.A.E.A.), IAEA, Vienna, pp. 159–170.

Gratier, J. P., Frery, E., Deschamps, P., Røyne, A., Renard, F., Dysthe, D., Ellouz-Zimmerman, N and **Hamelin, B.** (2012). How travertine veins grow from top to bottom and lift the rocks above them: The effect of crystallization force. *Geology*, **40**(11), 1015-1018.

Guo, L. and **Riding, R.** (1998) Hot-spring travertine facies and sequences, Late Pleistocene, Rapolano Terme, Italy. *Sedimentology*, **45**, 163-180.

Hansen, M., Dreybrodt, W., and **Scholz, D.** (2013). Chemical evolution of dissolved inorganic carbon species flowing in thin water films and its implications for (rapid) degassing of CO_2 during speleothem growth. *Geochimica et Cosmochimica Acta*, **107**, 242-251.

Hori, M., Kawai, T., Matsuoka, J., and **Kano, A.** (2009). Intra-annual perturbations of stable isotopes in tufas: effects of hydrological processes. *Geochimica et Cosmochimica Acta*, **73**(6), 1684-1695.

Huerta, P., Rodríguez-Berriguete, A., Martín-García, R., Martín-Pérez, A., La Iglesia Fernández, A. and **Alonso-Zarza, A.M.** (2015) The role of climate and aeolian dust input in calcrete formation in volcanic islands (Lanzarote and Fuerteventura, Spain). *Palaeogeography, Palaeockimatology, Palaeoecology*, **417**, 66-79.

Ibarra, Y., Corsetti, F. A., Feakins, S. J., Rhodes, E. J., and **Kirby, M. E.** (2015). Fluvial tufa evidence of Late Pleistocene wet intervals from Santa Barbara, California, USA. *Palaeogeography, Palaeoclimatology, Palaeoecology*, **422**, 36-45.

Jones, B. and **Renaut, R.W.** (2010) Calcareous spring deposits in continental settings. In: *Carbonates in Continental Settings. Facies Environments and Processes* (Eds. A.M. Alonso-Zarza, and L.H. Tanner). Elsevier, Amsterdam, 177-224.

Jones, B. and **Peng, X.** (2014) Hot spring deposits on a cliff face: A case study from Jifei, Yunnan Province, China. *Sedimentary Geology*, **302**, 1-28.

Kano, A., Matsuoka, J., Kojo, T., and **Fujii, H.** (2003). Origin of annual laminations in tufa deposits, southwest Japan. *Palaeogeography, Palaeoclimatology, Palaeoecology*, **191**(2), 243-262.

Kawai, T., Kano, A., and **Hori, M.** (2009). Geochemical and hydrological controls on biannual lamination of tufa deposits. *Sedimentary Geology*, **213**(1), 41-50.

Kele, S., Demény, A., Siklósy, Z., Németh, T., Mária, T., and **Kovács, M.B.** (2008) Chemical and stable isotope compositions of recent hot-water travertines and associated thermal waters, from Egerszalók, Hungary: depositional facies and non-equilibrium fractionations. *Sedimentary Geology*, **211**, 53–72.

Kele, S., Özkul, M., Fórizs, I., Gökgöz, A., Baykara, M.O., Alçiçek, M.C., and **Németh, T.** (2011) Stable isotope geochemical study of Pamukkale travertines: New evidences of low-temperature non-equilibrium calcite-water fractionation. *Sedimentary Geology*, **238**, 191-212.

Kele, S., Breitenbach, S. F., Capezzuoli, E., Meckler, A. N., Ziegler, M., Millan, I. M., Kluge, T., Deák, J., Hanselmann, K., John, C.M., Yan, H., Liu, Z., and **Bernasconi, S.M.** (2015). Temperature dependence of oxygen-and clumped isotope fractionation in carbonates: A study of travertines and tufas in the 6–95 C temperature range. *Geochimica et Cosmochimica Acta*, **168**, 172-192.

Kim, S. T., and **O'Neil, J. R.** (1997). Equilibrium and nonequilibrium oxygen isotope effects in synthetic carbonates. *Geochimica et Cosmochimica Acta*, **61**(16), 3461-3475.

Kluge, T., Affek, H. P., Dublyansky, Y., and **Spötl, C.** (2014). Devils Hole paleotemperatures and implications for oxygen isotope equilibrium fractionation. *Earth and Planetary Science Letters*, **400**, 251-260.

Liu, Z., Li, H., You, C., Wan, N., and **Sun, H.** (2006). Thickness and stable isotopic characteristics of modern seasonal climate-controlled sub-annual travertine laminas in a travertine-depositing stream at Baishuitai, SW China: implications for paleoclimate reconstruction. *Environmental Geology*, **51**(2), 257-265.

Liu, Z., Sun, H., Baoying, L., Xiangling, L., Wenbing, Y., and **Cheng, Z.** (2010). Wet-dry seasonal variations of hydrochemistry and carbonate precipitation rates in a travertine-depositing canal at Baishuitai, Yunnan, SW China: implications for the formation of biannual laminae in travertine and for climatic reconstruction. *Chemical Geology*, **273**(3), 258-266.

Lopez Gomez, A. (1972) El cultivo del plátano en Canarias. *Estudios Geográficos*, **33**, 5-68.

Matsuoka, J., Kano, A., Oba, T., Watanabe, T., Sakai, S., and **Seto, K.** (2001). Seasonal variation of stable isotopic compositions recorded in a laminated tufa, SW Japan. *Earth and Planetary Science Letters*, **192**(1), 31-44.

McCrea, J.M. (1950) On the isotope chemistry of carbonates and paleotemperature scale. *Journal of Chemical Physics*, **18**, 849-857.

Menéndez, I., Díaz-Hernández, J.L., Mangas, J., Alonso, I., and **Sánchez-Soto, P.J.** (2007) Airborne dust accumulation and soil development in the North-East sector of Gran Canaria (Canary Islands, Spain). *Journal of Arid Environments*, **71**, 57-81.

Mickler, P.J., Banner, J.L., Stern, L., Asmerom, Y., and **Edwards, R.L.** (2004) Stable isotope variations in modern tropical speleothems: Evaluating equilibrium vs. kinetic isotope effects. *Geochimica et Cosmochimica Acta*, **68**, 21, 4381-4393.

Mülinghaus, C., Scholz, D., and **Mangini, A.** (2009) Modelling fractionation of stable isotopes in stalagmites. *Geochimica et Cosmochimica Acta*, **73**, 7275-7289.

Muñoz, A., Bartolomé, M., Muñoz, A., Sancho, C., Moreno, A., Hellstrom, J. C., Osácar, M.C., and **Cacho, I.** (2015). Solar influence and hydrological variability during the Holocene from a speleothem annual record (Molinos Cave, NE Spain). *Terra Nova*, **27**(4), 300-311.

Myrttinen, A., Becker, V., and **Barth, J. A. C.** (2012). A review of methods used for equilibrium isotope fractionation investigations between dissolved inorganic carbon and CO_2. *Earth-Science Reviews*, **115**(3), 192-199.

Nielsen, L. C., DePaolo, D. J., and **De Yoreo, J. J.** (2012). Self-consistent ion-by-ion growth model for kinetic isotopic fractionation during calcite precipitation. *Geochimica et Cosmochimica Acta*, **86**, 166-181.

Okumura, T., Takashima, C., Shiraishi, F., Nishida, S., Yukimura, K., Naganuma, T., Koike, H., Arp, G., and **Kano, A.** (2011). Microbial processes forming daily lamination in an aragonite travertine, Nagano-yu Hot Spring, Southwest Japan. *Geomicrobiology Journal*, **28**(2), 135-148.

Okumura, T., Takashima, C., Shiraishi, F., Akmaluddin, and **Kano, A.** (2012) Textural transition in an aragonite travertine formed under various flow conditions at Pancuran Pitu, Central Java, Indonesia. *Sedimentary Geology*, **265**, 195–209.

Okumura, T., Takashima, C., and **Kano, A.** (2013)**a**. Textures and processes of laminated travertines formed by unicellular cyanobacteria in Myoken hot spring, southwestern Japan. *Island Arc*, **22**(3), 410-426.

Okumura, T., Takashima, C., Shiraishi, F., Nishida, S., and **Kano, A.** (2013)**b**. Processes forming daily lamination in a microbe-rich travertine under low flow condition at the Nagano-yu Hot Spring, southwestern Japan. *Geomicrobiology Journal*, **30**(10), 910-927.

O'Neil, J. R., Clayton, R. N., and **Mayeda, T. K.** (1969). Oxygen isotope fractionation in divalent metal carbonates. *The Journal of Chemical Physics*, **51**(12), 5547-5558.

Ordóñez, S., Martín, J. G., Del Cura, M. G., and **Pedley, H. M.** (2005). Temperate and semi-arid tufas in the Pleistocene to Recent fluvial barrage system in the Mediterranean area: The Ruidera Lakes Natural Park (Central Spain). *Geomorphology*, **69**, 332-350.

Passchier, C., Sürmelihindi, G., Spötl, C., Mertz-Kraus, R., & Scholz, D. (2016). Carbonate deposits from the ancient aqueduct of Béziers, France A high-resolution palaeoenvironmental archive for the Roman Empire. *Palaeogeography, Palaeoclimatology, Palaeoecology*, **461**, 328-340.

Pedley, M. (1990) Classification and environmental models of cool freshwater tufas. *Sedimentary Geology*, **68**, 143–154.

Pedley, M. (2009) Tufas and travertines of the Mediterranean region: a testing ground for freshwater carbonate concepts and developments. *Sedimentology*, **56**, 221-246

Pentecost, A. (2005) Travertine. 445 pp. Springer, Berlín.

Pentecost, A. and **Viles, H.** (1994) A Review and Reassessment of Travertine classification. *Geographie Physique Et Quaternaire*, **48**, 305-314.

Rimstidt, J.D., Balog, A., and **Webb, J.** (1998) Distribution of trace elements between carbonate minerals and aqueous solutions. *Geochimica et Cosmochimica Acta*, **11**, 1851-1863.

Roberts, M.S., Smart, P.L., and **Baker, A.,** (1998). Annual trace element variations in a Holocene speleothem. *Earth and Planetary Science Letters*, **154**, 237-246.

Rodríguez-Berriguete, Á. (2017) Petrología, sedimentología y geoquímica de los travertinos y tobas del Barranco de Azuaje (Gran Canaria): características e implicaciones. PhD Thesis (unpublished). Universidad Complutense de Madrid. 291 pp.

Rodríguez-Berriguete, Á., Alonso-Zarza, A.M., Cabrera, M.C., and **Rodríguez-González, A.** (2012) The Azuaje travertine: an example of aragonite deposition in a recent volcanic setting, N Gran Canaria Island, Spain. *Sedimentary Geology*, **277–278**, 61–71.

Rodríguez-Berriguete, Á., Alonso-Zarza, A. M., and **Martín-García, R.** (2017). Diagenesis of continental carbonate country rocks underlying surficial travertine spring deposits. *Quaternary International*, **437**, 4-14.

Rodríguez Lupiañez, G. (1967) Cultivo de la platanera. *Hojas Divulgadoras* (Ministerio de Agricultura de España), **17-18**, 24 pp.

Romanek, C.S., Grossman, E.L., and **Morse, J.W.** (1992) Carbon isotopic fractionation in synthetic aragonite and calcite: Effects on temperature and precipitation rate. *Geochimica et Cosmochimica Acta*, **56**, 419-430.

Romanov, D., Kaufmann, G., and **Dreybrodt, W.** (2008). $\delta^{13}C$ profiles along growth layers of stalagmites: comparing theoretical and experimental results. *Geochimica et Cosmochimica Acta*, **72**(2), 438-448.

Santamarta Cerezal, J. C. (2013). Hidrología y recursos hídricos en islas y terrenos volcánicos. Colegio de Ingenieros de Montes. 552 pp.

Saunders, P., Rogerson, M., Wadhawan, J. D., Greenway, G., and **Pedley, H. M.** (2014). Mg/Ca ratios in freshwater microbial carbonates: Thermodynamic, kinetic and vital effects. *Geochimica et Cosmochimica Acta*, **147**, 107-118.

SPA–15, (1975). Estudio cien fi co de los recursos de agua en las Islas Canarias (SPA/69/515). *Ministerio de Obras Públicas. Dirección General de Obras Hidráulicas. UNESCO.* Las Palmas de Gran Canaria, España.

Sürmelihindi, G., Passchier, C.W., Spötl, C., Kessener, P., Bestmann, M., Jacob, D.E., & Baykan, O.N. (2013). Laminated carbonate deposits in Roman aqueducts: Origin, processes and implications. *Sedimentology*, **60**(4), 961-982.

Tan, M., Baker, A., Genty, D., Smith, C., Esper, J., and **Cai, B.** (2006) Applications of stalagmite laminae to paleoclimate reconstructions: comparison with dendrochronology/climatology. *Quaternary Science Reviews*, **25**, 2103-2117.

Vázquez-Urbez, M., Arenas, C., and **Pardo, G.** (2012) A sedimentary facies model for stepped, fluvial tufa system in the Iberian Range (Spain): the Quaternary Piedra and Mesa valleys. *Sedimentology*, **59**, 502-526.

Yan, H., Sun, H., and **Liu, Z.** (2012). Equilibrium vs. kinetic fractionation of oxygen isotopes in two low-temperature travertine-depositing systems with differing hydrodynamic conditions at Baishuitai, Yunnan, SW China. *Geochimica et Cosmochimica Acta*, **95**, 63-78.

Zhang, D. D., Zhang, Y., Zhu, A., and **Cheng, X.** (2001). Physical mechanisms of river waterfall tufa (travertine) formation. *Journal of Sedimentary Research*, **71**(1), 205-216.

Figure Captions

Figure 1: A. Location of Canary Islands; B. Location of Gran Canaria. Squared area corresponds to study area; C. Wider view of squared area in b, showing the location of the Calabozo deposit and location of wells supplying water for the pipe system (coloured area). (A and B: modified from Google Maps (2016); C: modified from MDT05, © Instituto Geográfico Nacional de España)

Figure 2: A. Location of the Calabozo deposit within the ravine (dotted line). White arrow marks the position of the pipe; B. Detail of the pipe and the carbonate formed around it.

Figure 3: Transversal sketch of the deposit showing the main morphological elements: slopes, pools, and cascade-barriers. Numbers represent sampling points.

Figure 4: Field images showing: A. Slope encrusted by carbonate; B. Detail of the encrusted slope area where oncoid from (C) appeared; C. Oncoid with a nucleus made of EPS ©BASF; D. Detail from a pool showing terrigenous infilling; E, F. Cascade-barriers made of encrusted plant parts forming curtains and peaks.

Figure 5: A. Scanned thin section showing plant parts in life position encrusted by micritic calcite (red colour due to staining with Alizarin S); B. Coarse crystalline facies consisting on shrubby crystals crosscut by concentric lamination; C. SEM image of dendritic to columnar calcite crystal aggregates from coated stems; D. SEM image of dendritic to columnar calcite crystal aggregates with trigonal morphologies; E. SEM image of the coarse crystalline facies showing crystal aggregates with shrubby morphologies and interruptions visible within the crystal; F. SEM image of a filament encased by trigonal calcite crystals.

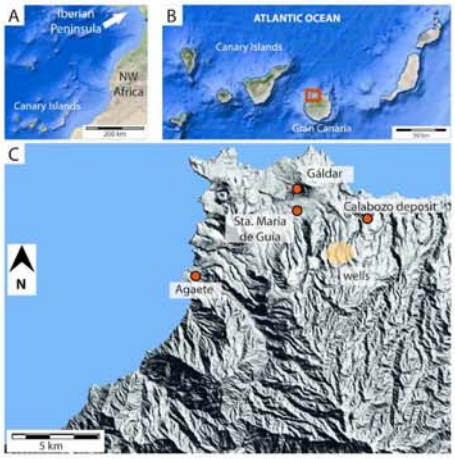

Figure 1: A. Location of Canary Islands; B. Location of Gran Canaria. Squared area corresponds to study area; C. Wider view of squared area in b, showing the location of the Calabozo deposit and location of wells supplying water for the pipe system (coloured area). (A and B: modified from Google Maps (2016); C: modified from MDT05, © Instituto Geográfico Nacional de España)

216x144mm (300 x 300 DPI)

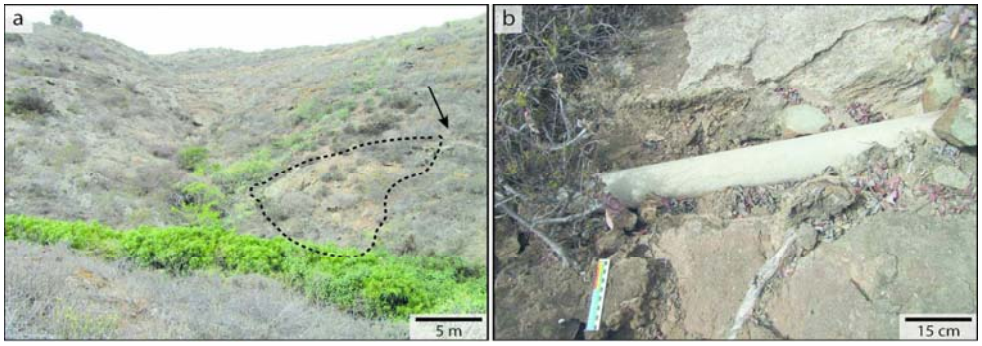

Figure 2: A. Location of the Calabozo deposit within the ravine (dotted line). White arrow marks the position of the pipe; B. Detail of the pipe and the carbonate formed around it.

170x59mm (300 x 300 DPI)

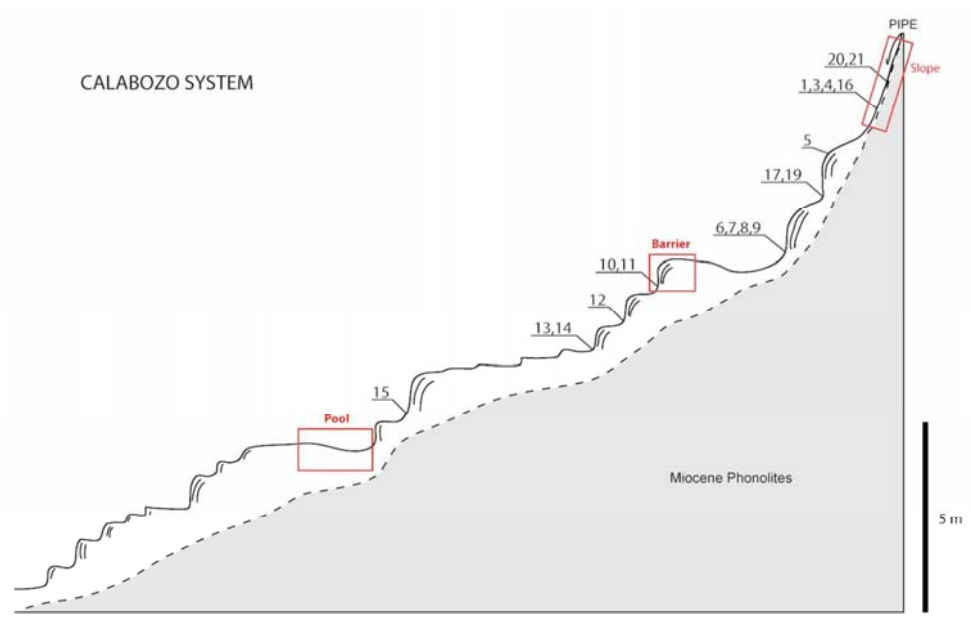

Figure 3: Transversal sketch of the deposit showing the main morphological elements: slopes, pools, and cascade-barriers. Numbers represent sampling points.

244x155mm (150 x 150 DPI)

Figure 4: Field images showing: A. Slope encrusted by carbonate; B. Detail of the encrusted slope area where oncoid from (C) appeared; C. Oncoid with a nucleus made of EPS ©BASF; D. Detail from a pool showing terrigenous infilling; E, F. Cascade-barriers made of encrusted plant parts forming curtains and peaks.

170x178mm (300 x 300 DPI)

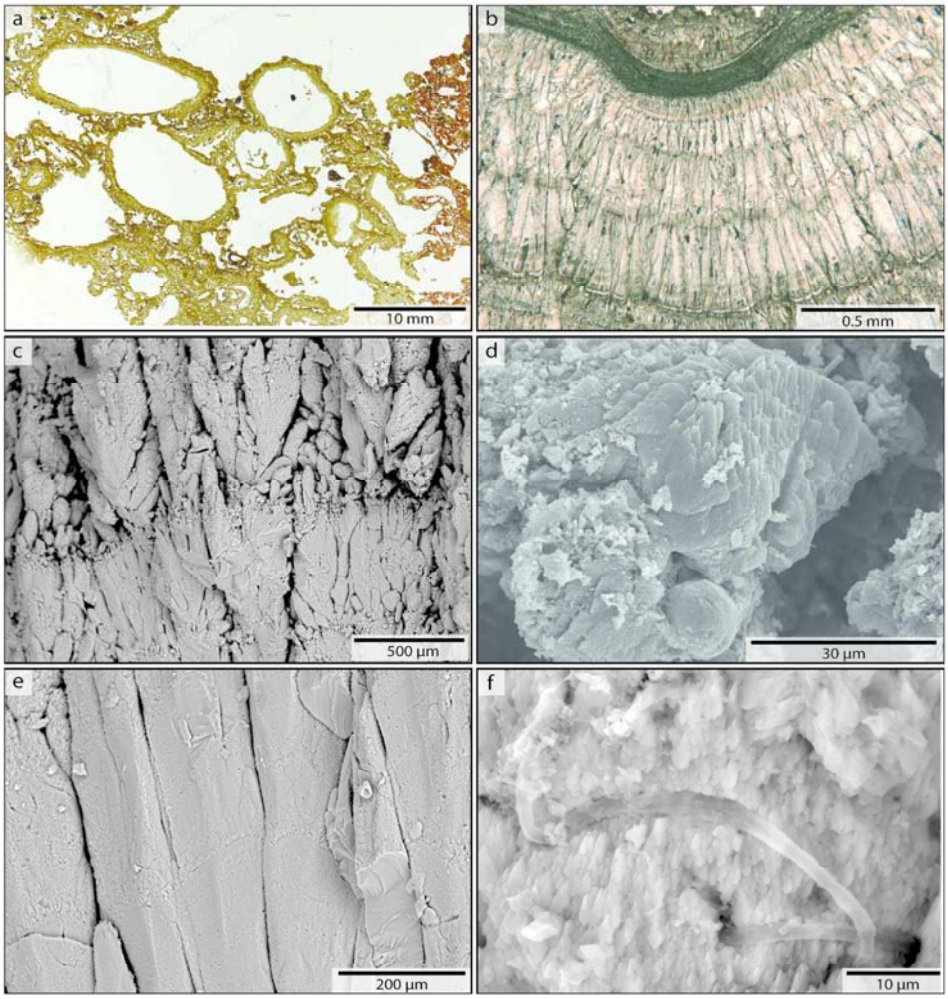

Figure 5: A. Scanned thin section showing plant parts in life position encrusted by micritic calcite (red colour due to staining with Alizarin S); B. Coarse crystalline facies consisting on shrubby crystals crosscut by concentric lamination; C. SEM image of dendritic to columnar calcite crystal aggregates from coated stems; D. SEM image of dendritic to columnar calcite crystal aggregates with trigonal morphologies; E. SEM image of the coarse crystalline facies showing crystal aggregates with shrubby morphologies and interruptions visible within the crystal; F. SEM image of a filament encased by trigonal calcite crystals.

176x192mm (300 x 300 DPI)

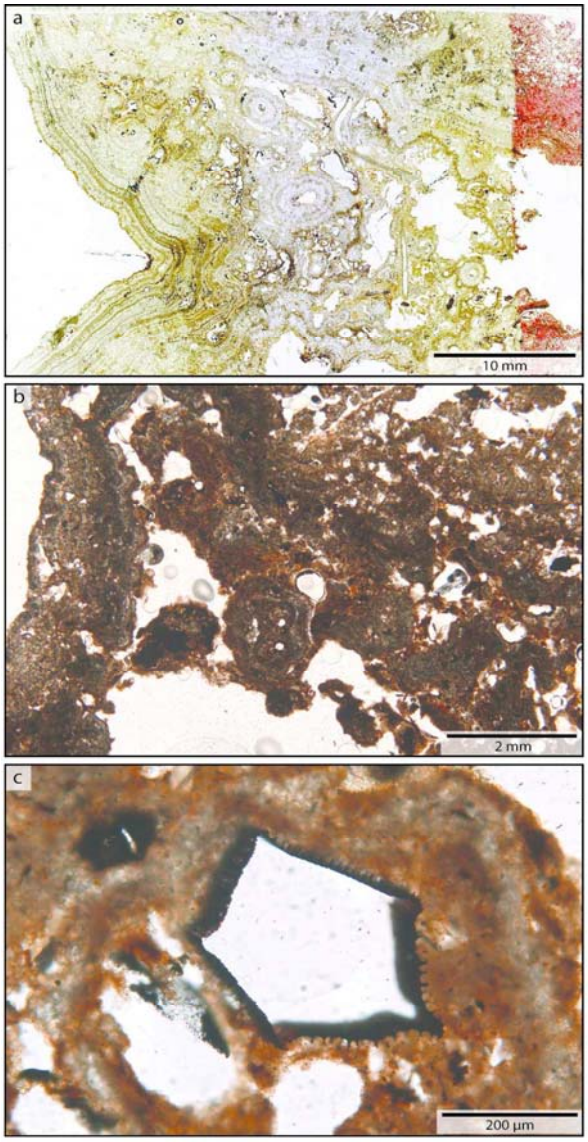

Figure 6: A. Scanned thin section showing crystalline crust facies (red colour due to staining with Alizarin S); B. Phytoclastic wackestone; C. Detail of a phytoclastic wackestone showing a pentagonal transversal section of a partially preserved phytoclast.

117x226mm (300 x 300 DPI)

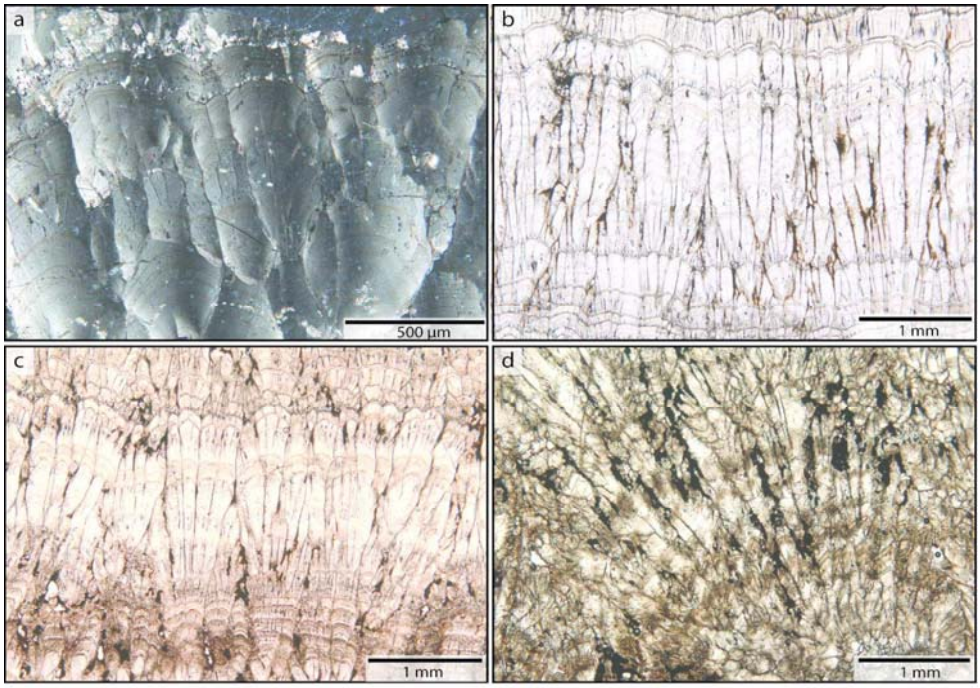

Figure 7: Images from optical microscope: A. Cone-shaped columnar crystals (polarised light); B. Cone-shaped columnar crystals with non to low branching on top; C. Columnar-branched crystals; D. Dendritic crystals.

170x123mm (300 x 300 DPI)

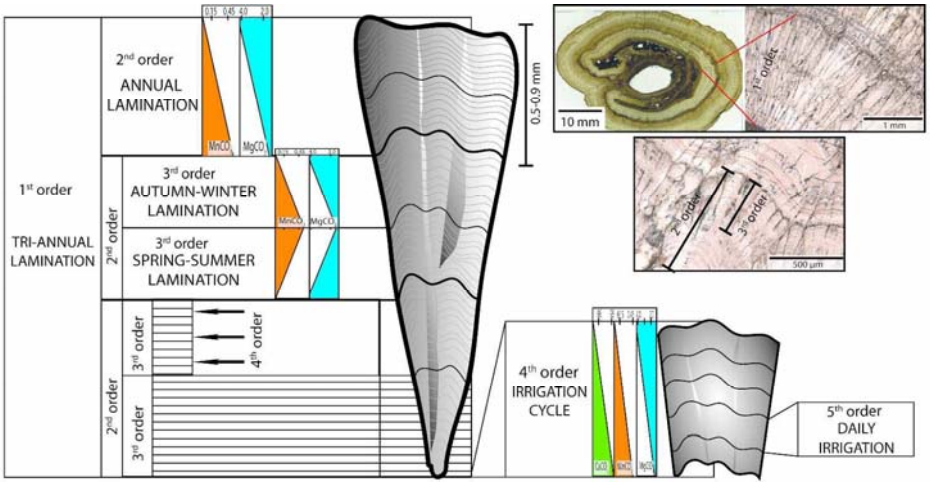

Figure 8: Sketch showing the hierarchy of the different orders of lamination and their geochemical variations. Images on upper right part correspond to scan of the studied thin section, and microscope images showing 1st to 3rd orders.

304x149mm (300 x 300 DPI)

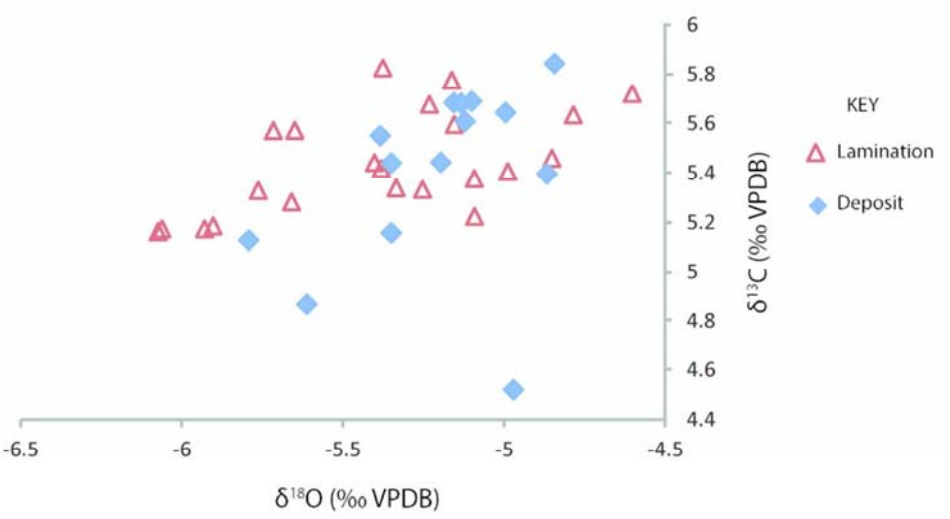

Figure 9: Stable isotopes from the whole deposit (blue rhombs) and the lamination (red triangles).

77x43mm (300 x 300 DPI)

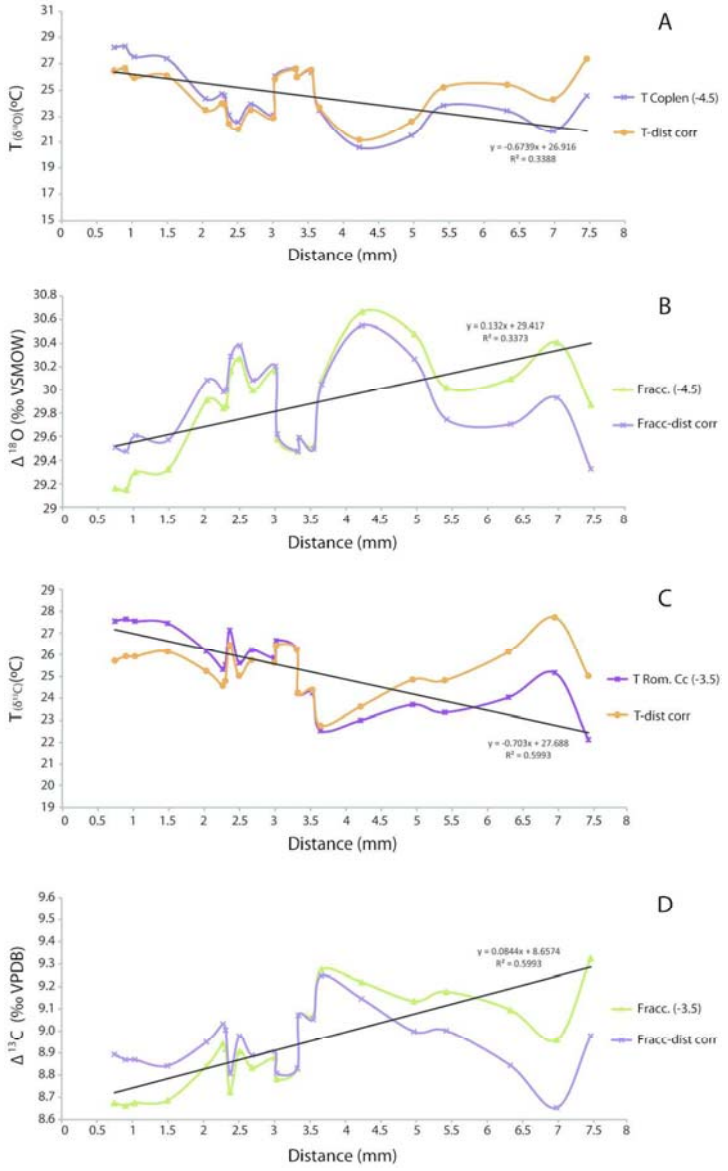

Figure 10: A. Calculated and corrected δ18O-based temperatures from lamination against distance; B. Calculated and corrected δ18O fractionation from lamination against distance; C. Calculated and corrected δ13C-based temperatures from lamination against distance; D. Calculated and corrected δ13C fractionation from lamination against distance.

112x182mm (300 x 300 DPI)

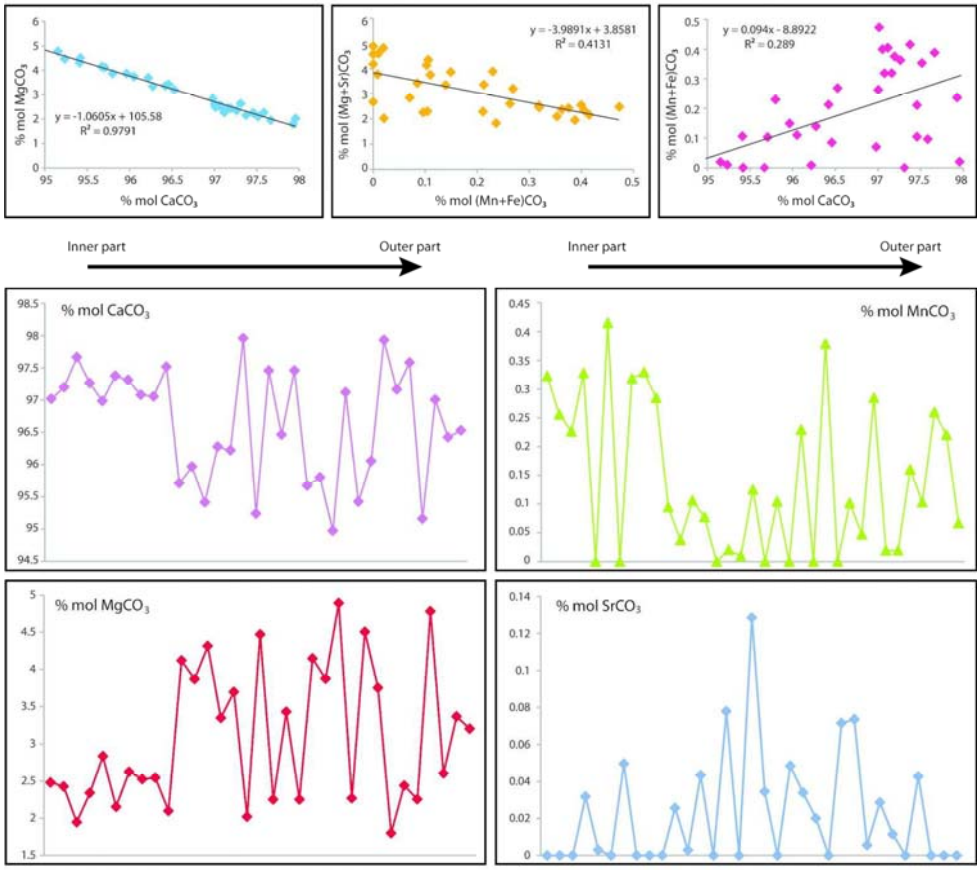

Figure 11: Geochemistry from laminated sample CAL-6: A. Mol percentage of CaCO3 plotted against mol percentage of MgCO3; B. Mol percentage of (Mn+Fe)CO3 plotted against mol percentage of (Mg+Sr)CO3; C. Mol percentage of CaCO3 plotted against mol percentage of (Mn+Fe)CO3; D. Mol percentage of CaCO3 plotted against distance; E. Mol percentage of MnCO3 plotted against distance; F. Mol percentage of MgCO3 plotted against distance; G. Mol percentage of SrCO3 plotted against distance

170x152mm (300 x 300 DPI)

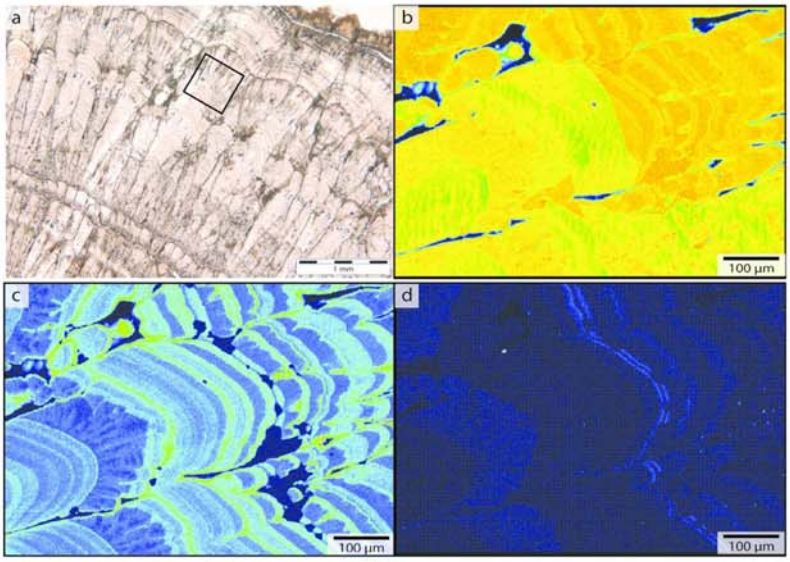

Figure 12: A. Microscope image showing the laminated sample analysed (square area: location of EMPA maps); Elemental maps from EMPA: B. Calcium; C. Magnesium; D. Manganese.

199x153mm (300 x 300 DPI)

SAMPLE	δ^{13}C cc(PDB)	distance (mm)	δ^{13}C CO_2(PDB)	Δcc-CO_2 (-3.50)	T(-3.5)	Δcorrected	Tcorrected
CAL6-10	5,17	0,75	-3,50	8,67	28	8,89	26
CAL6-3	5,16	0,90		8,66	28	8,87	26
CAL6-11	5,17	1,03		8,67	28	8,87	26
CAL6-31	5,19	1,49		8,69	27	8,84	26
CAL6-12	5,34	2,04		8,84	26	8,95	25
CAL6-4	5,44	2,28		8,94	25	9,03	25
CAL6-29	5,42	2,31		8,92	26	9,01	25
CAL6-5	5,22	2,38		8,72	27	8,81	26
CAL6-19	5,41	2,51		8,91	26	8,98	25
CAL6-30	5,33	2,69		8,83	26	8,89	26
CAL6-28	5,38	3,01		8,88	26	8,91	26
CAL6-13	5,28	3,03		8,78	27	8,81	26
CAL6-6	5,33	3,32		8,83	26	8,83	26
CAL6-14	5,57	3,34		9,07	24	9,07	24
CAL6-32	5,57	3,55		9,07	24	9,05	24
CAL6-15	5,77	3,66		9,27	23	9,25	23
CAL6-26	5,72	4,23		9,22	23	9,15	24
CAL6-7	5,63	4,97		9,13	24	9,00	25
CAL6-16	5,68	5,42		9,18	23	9,00	25
CAL6-8	5,59	6,33		9,09	24	8,84	26
CAL6-17	5,46	6,98		8,96	25	8,65	28
CAL6-18	5,82	7,46		9,32	22	8,98	25
MEAN	**5,44**			**8,94**	**25**	**8,94**	**25**

SAMPLE	δ^{18}Occ(SMOW)	distance (mm)	δ^{18}Ow(SMOW)	Δcc-w (-4.5)	T (-4.5)	Δcorrected	Tcorrected
CAL6-10	24,7	0,75	-4,50	29,16	28	29,50	26
CAL6-3	24,6	0,90		29,15	28	29,47	27
CAL6-11	24,8	1,03		29,30	28	29,60	26
CAL6-31	24,8	1,49		29,32	27	29,57	26
CAL6-12	25,4	2,04		29,91	24	30,08	24
CAL6-4	25,3	2,28		29,84	25	29,98	24
CAL6-29	25,4	2,31		29,86	25	30,00	24
CAL6-5	25,7	2,38		30,16	23	30,29	22
CAL6-19	25,8	2,51		30,27	23	30,38	22
CAL6-30	25,5	2,69		30,00	24	30,08	24
CAL6-28	25,7	3,01		30,16	23	30,21	23
CAL6-13	25,1	3,03		29,58	26	29,62	26
CAL6-6	25,0	3,32		29,47	27	29,47	27
CAL6-14	25,1	3,34		29,59	26	29,59	26
CAL6-32	25,0	3,55		29,52	26	29,49	27
CAL6-15	25,6	3,66		30,09	23	30,05	24
CAL6-26	26,2	4,23		30,67	21	30,55	21
CAL6-7	26,0	4,97		30,48	22	30,26	23
CAL6-16	25,5	5,42		30,02	24	29,74	25
CAL6-8	25,6	6,33		30,10	23	29,70	25
CAL6-17	25,9	6,98		30,41	22	29,93	24
CAL6-18	25,4	7,46		29,87	25	29,33	27
MEAN	**25,4**			**29,86**	**25**	**29,86**	**25**

Table 1: Calculated temperatures and isotope fractionations, and their respective corrections for both δ13C and δ18O stable isotopes from lamination.

171x200mm (300 x 300 DPI)

%weight	CaO	MgO	MnO	FeO	SrO	Al_2O_3	Total
	53,4580	0,9830	0,2250	0,1060	0,0000	0,0100	54,7820
	55,2390	0,9920	0,1840	0,0870	0,0000	0,0000	56,5020
	53,4650	0,7660	0,1570	0,1130	0,0000	0,0000	54,5010
	54,5770	0,9440	0,2330	0,0250	0,0330	0,0000	55,8120
	53,9370	1,1340	0,0000	0,0500	0,0030	0,0370	55,1610
	54,1180	0,8610	0,2920	0,0000	0,0000	0,0180	55,2890
	54,0930	1,0500	0,0000	0,0000	0,0510	0,0040	55,1980
	53,9590	1,0100	0,2240	0,0000	0,0000	0,0250	55,2180
	54,1940	1,0220	0,2330	0,0500	0,0000	0,0000	55,4990
	55,5290	0,8590	0,2050	0,0500	0,0000	0,0110	56,6540
	54,4580	1,6850	0,0680	0,0060	0,0270	0,0150	56,2590
	54,5040	1,5790	0,0270	0,0810	0,0030	0,0050	56,1990
	53,4350	1,7370	0,0750	0,0000	0,0450	0,0420	55,3340
	53,2900	1,3320	0,0540	0,0440	0,0000	0,0800	54,8000
	54,1720	1,4950	0,0000	0,0060	0,0810	0,0000	55,7540
	53,0740	0,7870	0,0140	0,0000	0,0000	0,0000	53,8750
	54,5470	1,8410	0,0070	0,0000	0,1360	0,0540	56,5850
	54,8370	0,9110	0,0890	0,0620	0,0360	0,0150	55,9500
	55,0430	1,4060	0,0000	0,0620	0,0000	0,0090	56,5200
	55,3770	0,9200	0,0750	0,0000	0,0510	0,0470	56,4700
	54,8950	1,7110	0,0000	0,0000	0,0360	0,0510	56,6930
	54,0840	1,5710	0,1640	0,0000	0,0210	0,0270	55,8670
	54,6700	2,0240	0,0000	0,0000	0,0000	0,0480	56,7420
	55,1200	0,9260	0,2720	0,0190	0,0750	0,0470	56,4590
	54,7640	1,8590	0,0000	0,0000	0,0780	0,0000	56,7010
	55,9510	1,5700	0,0750	0,0060	0,0060	0,0290	57,6370
	55,4810	0,7330	0,0340	0,1370	0,0300	0,0020	56,4170
	55,2680	0,9980	0,2050	0,0250	0,0120	0,0230	56,5310
	55,4810	0,9220	0,0140	0,0560	0,0000	0,0220	56,4950
	54,0950	1,9540	0,0140	0,0000	0,0450	0,0000	56,1080
	55,4580	1,0710	0,1160	0,0750	0,0000	0,0440	56,7640
	55,5660	1,3940	0,0750	0,0810	0,0000	0,0000	57,1160
	53,6550	1,2800	0,1830	0,0060	0,0000	0,0000	55,1240
MEAN	54,5392	1,2523	0,1004	0,0348	0,0233	0,0202	
MEDIAN	54,5470	1,0710	0,0750	0,0190	0,0030	0,0150	
MAX.	55,9510	2,0240	0,2920	0,1370	0,1360	0,0800	
MIN.	53,0740	0,7330	0,0000	0,0000	0,0000	0,0000	
RANGE	2,8770	1,2910	0,2920	0,1370	0,1360	0,0800	
STD. DEV.	0,7709	0,3884	0,0956	0,0400	0,0326	0,0214	

%mol	%mol $CaCO_3$	%mol $MgCO_3$	%mol$MnCO_3$	%mol $FeCO_3$	%mol $SrCO_3$	%molAlOOH	total
	97,0154	2,4817	0,3228	0,1502	0,0000	0,0299	100
	97,1963	2,4282	0,2559	0,1195	0,0000	0,0000	100
	97,6656	1,9466	0,2267	0,1611	0,0000	0,0000	100
	97,2647	2,3404	0,3283	0,0348	0,0318	0,0000	100
	96,9806	2,8365	0,0000	0,0702	0,0029	0,1098	100
	97,3780	2,1552	0,4154	0,0000	0,0000	0,0534	100
	97,3107	2,6278	0,0000	0,0000	0,0497	0,0119	100
	97,0793	2,5279	0,3186	0,0000	0,0000	0,0742	100
	97,0540	2,5462	0,3299	0,0699	0,0000	0,0000	100
	97,5164	2,0986	0,2846	0,0685	0,0000	0,0319	100
	95,7084	4,1197	0,0945	0,0082	0,0257	0,0435	100
	95,9661	3,8677	0,0376	0,1113	0,0029	0,0145	100
	95,4122	4,3147	0,1059	0,0000	0,0435	0,1237	100
	96,2746	3,3477	0,0771	0,0620	0,0000	0,2385	100
	96,2197	3,6941	0,0000	0,0083	0,0779	0,0000	100
	97,9588	2,0208	0,0204	0,0000	0,0000	0,0000	100
	95,2347	4,4715	0,0097	0,0000	0,1285	0,1556	100
	97,4580	2,2524	0,1250	0,0860	0,0346	0,0440	100
	96,4614	3,4278	0,0000	0,0848	0,0000	0,0260	100
	97,4582	2,2524	0,1043	0,0000	0,0486	0,1365	100
	95,6710	4,1483	0,0000	0,0000	0,0340	0,1467	100
	95,8001	3,8712	0,2297	0,0000	0,0201	0,0789	100
	94,9711	4,8914	0,0000	0,0000	0,0000	0,1376	100
	97,1171	2,2697	0,3789	0,0261	0,0715	0,1366	100
	95,4203	4,5061	0,0000	0,0000	0,0736	0,0000	100
	96,0529	3,7495	0,1018	0,0080	0,0056	0,0821	100
	97,9294	1,7999	0,0474	0,1888	0,0287	0,0058	100
	97,1619	2,4408	0,2849	0,0343	0,0114	0,0667	100
	97,5838	2,2560	0,0195	0,0769	0,0000	0,0638	100
	95,1560	4,7817	0,0195	0,0000	0,0428	0,0000	100
	97,0041	2,6061	0,1604	0,1024	0,0000	0,1270	100
	96,4222	3,3652	0,1029	0,1097	0,0000	0,0000	100
	96,5278	3,2035	0,2603	0,0084	0,0000	0,0000	100
MEAN	96,6494	3,0802	0,1413	0,0482	0,0222	0,0588	
MEDIAN	97,0041	2,6278	0,1029	0,0261	0,0029	0,0435	
MAX.	97,9588	4,8914	0,4154	0,1888	0,1285	0,2385	
MIN.	94,9711	1,7999	0,0000	0,0000	0,0000	0,0000	
RANGE	2,9878	3,0915	0,4154	0,1888	0,1285	0,2385	
STD. DEV.	0,8672	0,9294	0,1350	0,0556	0,0310	0,0625	

Table 2: Geochemical data obtained through EMPA (%weight) and recalculations to %mol of the respective carbonates.

243x135mm (300 x 300 DPI)

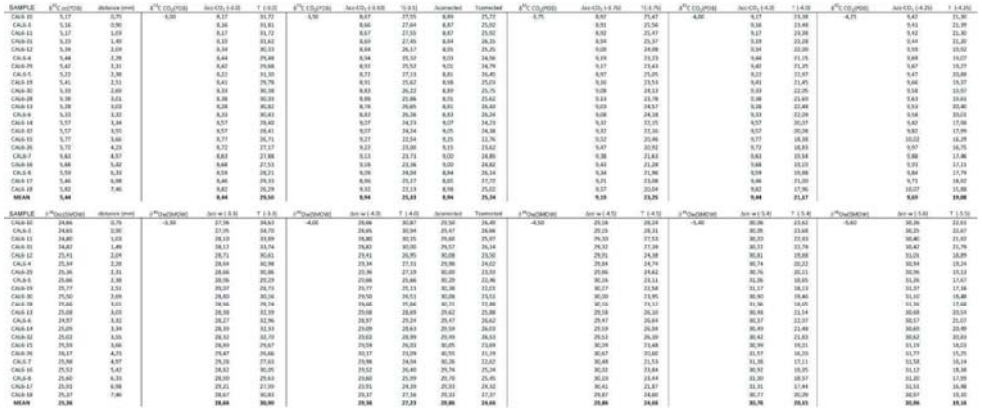

284x118mm (300 x 300 DPI)